

INVESTIGATION OF THE POTENTIAL  
EFFECTS OF BONE TURNOVER ON  
X-RAY FLUORESCENCE  
MEASUREMENTS OF BONE LEAD IN  
YOUNG WOMEN

THE EFFECTS OF BONE TURNOVER  
ON BONE LEAD MEASUREMENTS  
OF YOUNG WOMEN THROUGH X-  
RAY FLUORESCENCE

By BRENDAN SHEEHAN, B.Sc.

A Thesis Submitted to the School of Graduate Studies in Partial Fulfilment  
of the Requirements for  
the Degree Master of Science

McMaster University © Copyright by Brendan Sheehan, Sept 2022

McMaster University MASTER OF SCIENCE (2022) Hamilton, Ontario (Radiation Biology)

TITLE: Investigation of the potential effects of bone turnover on x-ray fluorescence measurements of bone lead in young women

AUTHOR: Brendan Sheehan B.Sc.

SUPERVISOR: Professor F. E. McNeill

NUMBER OF PAGES: x, 70

## Abstract

The potential effect of bone turnover on bone lead k X-Ray Fluorescence (XRF) measurements in young women were examined in this thesis. Published data has shown that men and women do not release lead back into blood from bone stores at the same rate until after menopause. Recently our laboratory re-investigated this phenomenon, and currently unpublished data showed that the release rate for young women may be better modelled through a non-linear function. One possible explanation is sex differences in cortical porosity. However, it was unknown whether cortical porosity could create a measurement artifact. Using 3D printing techniques, a phantom design was created that emulates cortical porosity at structural sizes of 300 microns. A calibration set of lead-doped cortical porosity phantoms were created and compared with past bone lead phantoms, there was no statistically significant differences observed. In phantoms with homogenous distributions of lead, cortical porosity does not appear to affect phantom measurements. Monte-Carlo simulations were performed using MCNP to verify and expand upon these results. Findings agreed with experimental results, and it was also shown that heterogenous distribution of lead did not affect K-XRF measurements until the distributions were extreme. Cortical porosity does not appear to result in XRF measurement artifacts, and the non-linearity in the relationship between blood and bone levels observed in young women appears to be real. Published analysis of in vivo data sets of young women found measurements in morbidly obese women were inaccurate. The effect of soft tissue overlay on bone lead measurements was therefore examined using MCNP. Results showed as soft tissue overlay thickness increases, the average measured bone lead value decreases. MCNP further showed that while the measured bone lead level in an individual is reduced, an increase in measurement uncertainty measurement masked the reduction. This may explain why the phenomenon has not been clearly observed and understood until now.

## Acknowledgments

I would like to thank first and foremost Dr. Fiona McNeill, for making my graduate school experience smooth and stress free through a global pandemic. You went above and beyond my expectations of how kind and helpful a supervisor could be.

Thank you, Renée Bider, without you I would still be trying to find my way around campus and the laboratory.

I would also like to thank Erin, my partner for giving me the belief I need to accomplish my goals.

Finally, I would like to thank my family for always supporting me throughout this journey.

## Table of Contents

Abstract.....	iii
Acknowledgments .....	iv
List of Tables and Figures .....	vii
Declaration of Academic Achievement .....	x
<b>1. Introduction.....</b>	<b>1</b>
1.1. Scope of Thesis .....	1
1.2. X-Ray Fluorescence (XRF) .....	2
1.3. Compton Scattering.....	4
1.4. Coherent Scattering.....	4
1.5. Normalization.....	5
1.6. The Development and Application of XRF based bone lead measurement systems .....	6
1.7. Lead metabolism .....	9
1.8. Bone metabolism .....	13
1.9. Cortical Porosity .....	14
<b>2. Methods of Experimental Porous Bone Phantom.....</b>	<b>18</b>
2.1. Creating a 3D printable porous bone model .....	18
2.2. Filling a 3D printable porous bone model .....	23
2.3. Measuring and analyzing bone lead phantoms.....	25
<b>3. Results and Discussion of Porous Bone Phantom .....</b>	<b>30</b>

3.1.	Cylindrical tibia phantom measurements and calibration line.....	30
3.2.	Lattice tibia phantom measurements and calibration line .....	33
4.	Methods of Monte Carlo Simulations of Porous Bone Phantom.....	39
4.1.	Recreating models in MCNP .....	39
4.2.	Testing the effect of bone lead distributions in MCNP .....	43
4.3.	Testing the effect of tissue overlay in obese subjects in MCNP.....	47
5.	Results and Discussion of Monte Carlo Simulations of Porous Bone Phantom.....	49
5.1.	MCNP simple tibia phantom measurements and calibration line .....	49
5.2.	MCNP lattice phantom measurements and calibration line.....	52
5.3.	MCNP changes in the distribution of lead in bone .....	54
5.4.	Soft tissue versus alpha/coherent ratio .....	57
6.	Conclusions and Future Work.....	59
	Bibliography .....	64

## List of Tables and Figures

Figure 1.1 Photoelectric absorption vs photon energy for Lead (M.J. Berger et al., 2010). .....	3
Figure 1.2 Biokinetic model of lead in the human body. Figure created by ©Fiona McNeill .....	11
Figure 1.3 Endogenous exposure of lead versus age for young men and women. Figure created by ©Fiona McNeill .....	12
Figure 1.4. Endogenous exposure of lead versus age for young men and women. Figure created by ©Fiona McNeill .....	12
Table 1-1 Comparison of endogenous lead exposure rate for different groups (Popovic et al., 2005) .....	13
Figure 1.5 “Idealized structure of cortical BMU in longitudinal section, showing cutting cone, reversal zone and closing cone. (Smith et al., 2012)” .....	15
Figure 1.6 From “Spatial distribution of the trace elements zinc, strontium and lead in human bone tissue”, p. 188, by (Pemmer et al., 2013). “Examples of qBEI images with corresponding SR $\mu$ -XRF element maps of Ca, Zn, Pb, Sr: (a) osteonal bone region of the human femoral neck. The color-coded X-ray intensities are normalized to counts per second (cps), 100 mA Ring current and are scaled from minimum to maximum within each individual map. qBEI images show younger bone packets (less mineralized) as darker, and older bone packets (more mineralized) as brighter gray levels. Sample (b) exhibiting multiple parallel cement lines.” .....	16
Figure 2.1 Unsuccessfully 3D printed lattice structure.....	22
Figure 2.2 Successfully 3D printed Lattice structure.....	22
Figure 2.3 3D printed cube for housing lattice structure. ....	22
Table 2-1 Material weights for lead plaster of Paris phantoms. ....	23
Figure 2.4 Cross section of filled lattice phantom. ....	25
Figure 2.5 $^{109}\text{Cd}$ decay scheme (Xiaolong et al., 2010).....	26
Figure 2.6 Sample detector spectrum from $^{109}\text{Cd}$ bone lead XRF system.....	26
Figure 2.7 Curve fitting of Coherent area of spectrum using Origin © software. ....	27
Figure 2.8 Curve fitting of $K_{\alpha 1}$ and $K_{\alpha 2}$ area of spectrum using Origin © software. ....	28
Table 3-1 The mass attenuation coefficient and x-ray interaction cross-sections ( $\text{cm}^2/\text{g}$ ) for soft tissue and HPDE at significant x ray energies for lead K-XRF measurements (ICRU, 1989).....	30

Table 3-2 Pb $K_{\alpha 1}$ peak area/coherent peak area from this work and Behinaein et al., 2011. ....	31
Figure 3.1 Pb concentration vs. Pb $K_{\alpha 1}$ peak area/coherent peak area for cylindrical phantoms.	32
Figure 3.2 Pb concentration vs. average Pb $K_{\alpha 1}$ peak area/coherent peak area for cylindrical phantoms. ....	33
Figure 3.3 Pb concentration vs. Pb $K_{\alpha 1}$ peak area/coherent peak area for lattice phantom.....	35
Figure 3.4 Pb concentration vs. Pb $K_{\alpha 1}$ peak area/coherent peak area for lattice phantom.....	36
Figure 3.5 Pb concentration vs Pb $K_{\alpha 1}$ peak area/coherent peak area for lattice phantoms .....	37
Figure 3.6 Pb concentration vs Pb $K_{\alpha 1}$ peak area/coherent peak area for lattice phantoms from batch 1 and 2 .....	38
Figure 4.1 XRF system replicated in MCNP with a simple cylindrical bone lead phantom. ....	41
Figure 4.2 2-D view of lattice phantom in MCNP.....	41
Figure 4.3 2-D view of lattice phantom “1x1” created in MCNP. ....	44
Figure 4.4 2-D view of lattice phantom “2x2” created in MCNP. ....	45
Figure 4.5 2-D view of lattice phantom “4x4” created in MCNP. ....	46
Figure 4.6 2-D view of lattice phantom “11x11” created in MCNP. ....	46
Figure 4.7 2-D view of cylindrical plaster phantom with 0 cm of soft tissue created in MCNP..	47
Figure 4.8 2-D view of cylindrical plaster phantom with 5 cm of soft tissue created in MCNP..	48
Figure 5.1 Pb concentration vs Pb $K_{\alpha 1}$ peak area/coherent peak area for cylindrical phantom in MCNP. ....	51
Figure 5.2 Pb concentration vs Pb $K_{\alpha 1}$ peak area/coherent peak area for cylindrical phantom in MCNP. ....	52
Figure 5.3 Pb concentration vs Pb $K_{\alpha 1}$ peak area/coherent peak area for lattice phantoms in MCNP. ....	53
Figure 5.4 Pb concentration vs Pb $K_{\alpha 1}$ peak area/coherent peak area for cylindrical and lattice phantoms in MCNP. ....	54
Figure 5.5 2-D view of lattice phantoms, from left to right: “1x1”, “2x2”, “4x4”, “11x11”. ....	56
Figure 5.6 Consecutive cubes of Pb-doped bone material vs Pb $K_{\alpha 1}$ peak area/coherent peak area for cylindrical and lattice phantoms in MCNP. ....	57

Figure 6.1 Thickness of soft tissue vs. Pb  $K_{\alpha 1}$  peak area/coherent peak area. .... 61

Figure 6.2 Thickness of soft tissue vs. Pb  $K_{\alpha 1}$  peak area/coherent peak area with non-linear fit. 62

Figure 6.3 Bone Pb ( $\mu\text{g Pb/g bone mineral}$ ) versus Body Mass Index. .... 63

## Declaration of Academic Achievement

I declare the work completed in the thesis “Investigation of the potential effects of bone turnover on x-ray fluorescence measurements of bone lead in young women” for partial fulfillment of Master of Science is my own original work and does not include any plagiarism.

# 1. Introduction

## 1.1. Scope of Thesis

The scope of this thesis is to determine if bone turnover artifacts affect bone lead XRF measurements in young women. Endogenous Pb exposure, determined by plotting blood lead against bone lead in people with low current exposure, shows a linear relationship for men and postmenopausal women. However, in young women, recent re-analysis of data in our laboratory has found a change in the endogenous exposure rate, i.e., blood lead level per unit bone lead, with age between the ages of 20 and 35. As discussed in the following sections, this thesis examined if cortical porosity could play a role in these findings.

In order to study the affect of cortical porosity, the feasibility of creating a bone lead phantom which emulates cortical porosity was studied. Following this, a calibration set of bone lead phantoms was created to compare with past, simple bone lead phantoms. The phantom designs were further examined through the use of Monte Carlo simulation software. With this software, further designs were studied that would be not possible or impractical to create in a laboratory setting. In order to explain this problem and its challenges more thoroughly, the following sections of the introduction provide some necessary background information.

## 1.2. X-Ray Fluorescence (XRF)

X-ray fluorescence is a non-destructive analysis technique used to identify the elemental composition of materials. It is based on the photoelectric effect. When x-ray photons interact with matter, there is a possibility of photoelectric absorption, that depends on the atomic number of the element and the energy of the x-ray.

Photons can interact with inner shell electrons. If the energy of the photon is greater than the binding energy of the electron, it can be ejected. This ejected electron is referred to as a photoelectron, and has the energy of the incident photon, less the binding energy of the electron. As a result of the ejection of the electron, the atom is in an excited state, with a vacancy in the shell. To return to a lower excitation state, an electron from a higher shell can transition to fill the vacancy, moving from a higher to lower energy state. The excess energy, or the difference in energy between the two electron shells can be emitted in the form of a photon or an Auger electron. This photon is called a characteristic x-ray. Because the electron shell energies depend on the element, each element emits x-rays with specific energies, and thus the energy of the photon allows for element identification. An important factor in the feasibility of elemental analysis by XRF is the fluorescence yield. The fluorescence yield is the ratio of photons absorbed to the number of photons emitted through fluorescence. Elements with low atomic numbers have a lower fluorescence yield and thus emit fewer characteristic x-rays per photoelectric interaction. Lead has a high fluorescence yield, > 90%, and so is ideally suited to measurement by x-ray fluorescence.

The probability of photoelectric absorption depends on the atomic number of the material, increasing in probability as the atomic number increases. In addition, as the energy of the incident photon increases, the probability of photoelectric absorption generally decreases. However, as seen in figure 1.1 below, there are increases in the probability of photoelectric absorption at specific energies: these increases are at the binding energy of the electron shells of the element.

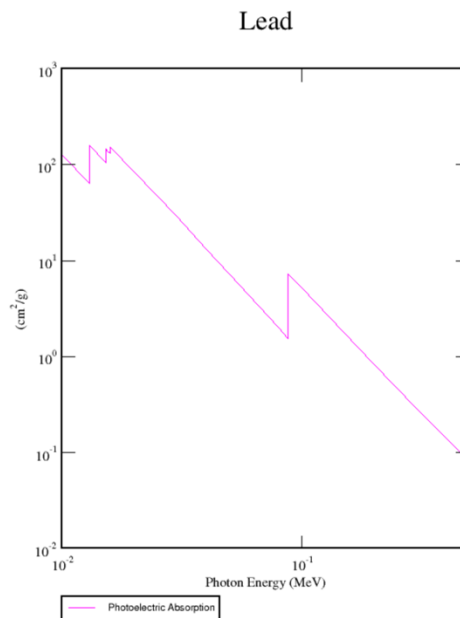


Figure 1.1 Photoelectric absorption vs photon energy for Lead (M.J. Berger et al., 2010).

As previously mentioned, depending on the electron ejected, and which outer shell electron moves down to fill the vacancy, a specific energy of photon will be released. Characteristic x-ray photons are therefore named according to these factors. For the purposes of this work with Pb, K $\alpha$  characteristic x-rays were studied. The “K” in K $\alpha$  represents that the electron was ejected from the K shell. The “ $\alpha$ ” signifies that the electron that filled the vacancy

was from 1 shell above the K shell, in this case the L shell. Depending on the subshell levels, this naming convention can be further descriptive, such as  $K\alpha_1$  and so on.

For a K shell electron to be emitted from a Pb atom, the energy of the photon incident on the material must be above the binding energy of this shell, also known as the K-edge. In this case, that energy is 88.005 keV. This makes Cd-109 an ideal source as it produces a gamma ray with an energy of 88.035 keV, just above the K-edge and thus at an energy where the cross-section has dramatically increased.

### 1.3. Compton Scattering

Compton scattering occurs when a photon interacts with an electron, causing the direction and energy of the photon to change. The energy lost from the photon, is imparted onto the electron based on conservation of energy and momentum. Depending on the angle of deflection of the incoming photon, this will determine the energy and angle the electron is ejected. As seen in table 3.1, incoherent scattering, or Compton scattering is the most dominant interaction in soft tissues in the relevant energy range of the K-XRF Pb system using a  $^{109}\text{Cd}$  source. For  $^{109}\text{Cd}$  K-XRF measurements, Compton scattering makes up the majority of the background spectrum for the  $K_{a1}$  peak and  $K_{a2}$  peak section.

### 1.4. Coherent Scattering

Coherent scatter, or elastic scattering occurs when a photon interacts with a material, causing the direction of the photon to change, while the energy of this photon remains equal

to the energy before the interaction. The probability of this interaction occurring increases as the atomic number ( $Z$ ) increases. At 88 keV, the energy used in the K-XRF bone lead system, the cross section for coherent scattering is 28 times higher for bone versus tissue (Keldani et al., 2017). There is only a small difference in energy between the coherent scatter x ray and the Pb K x-ray and this the attenuation of these photons through material is almost identical.

### 1.5. Normalization

When measuring the quantity of Pb in bone using  $^{109}\text{Cd}$  K XRF, it is essential to accurately quantify the amount of Pb relative to the individual and material. Between different people, there will be variation in bone concentration, as well as soft tissue thickness, position, bone shape and size. In addition, subjects are not restrained during the measurement, so there can be some motion by the volunteer. For this particular XRF technique using  $^{109}\text{Cd}$ , the lead signal is normalized to the coherent scatter signal, and it is generally assumed that this allows the measurement to be independent of bone tissue density and soft tissue overlay thickness. The normalization assumes that the Pb x-ray photons and the elastic scattered photons arise out of the same incident flux. This assumption holds if the lead x-ray photons are produced only by unscattered photons and the lead and bone material are identically distributed since the gamma ray emitted from  $^{109}\text{Cd}$  is only slightly above the K-edge of Pb, the majority of Pb K x-rays will be from primary interactions (Somervaille et al., 1985). It has, until now, been assumed that because the Pb and coherent x-rays can interrogate 1-2 cm of tissue, that the micro distribution of lead in bone does not matter. The normalization

has thus been used and this allows for the bone lead levels to be quantified in lead per quantity of bone.

### 1.6. The Development and Application of XRF based bone lead measurement systems

The first in-vivo bone lead measurements were performed the 1970's (Ahlgren et al., 1979). These measurements were performed on fingers and the tibia using a  $^{57}\text{Co}$  source and Ge(Li) detectors. The  $^{109}\text{Cd}$  K XRF system was then developed and replaced the earlier  $^{57}\text{Co}$  system because the normalization made accurate measurements easier to perform. Since this time, several different  $^{109}\text{Cd}$  systems have been designed to optimize these measurements. Currently, at McMaster University, an XRF system has been designed using a  $^{109}\text{Cd}$  source and 4 high purity germanium detectors (Nie et al., 2006a).

This experimental bone lead measurement system has been modelled in this thesis using the Monte Carlo code MCNP. Monte Carlo simulations are a method of analysis that uses a large number of iterations to measure an outcome, based on set probabilities for these interactions. Monte Carlo N-Particle code, or MCNP<sup>®</sup> is a Monte Carlo radiation transport code for photons, neutrons and electrons interactions. (Werner, 2018). MCNP is able to depict interactions of radiation with a variety of materials, these interactions include characteristic radiation. This allows it to be used to study x-ray fluorescence. MCNP has the ability to emulate a vast quantity of geometries and materials, through its generalized

input parameters, allowing the investigation of geometries or situations that may not be feasible or reasonable to conduct experimentally (Trojek & Čechák, 2007).

Plaster of Paris has long been used as a substitute for bone in medical applications and medical physics models (Gordon et al., 1993; Jamali et al., 2002) and <sup>109</sup>Cd bone lead systems have been calibrated using plaster of Paris phantoms since the 1980s (Somervaille et al 1985). Plaster of Paris is not a perfect match to the calcium hydroxyapatite in bone mineral, but it does have a similar linear attenuation coefficient to bone, and while its coherent scattering cross section is 21% higher than cortical bone (Somervaille et al., 1985), this difference can be corrected for (Somervaille et al, (1985)). Plaster of Paris is an inexpensive, easy to work with material that can be doped with lead using standard addition techniques. It can be poured into moulds of any shape. This allows it to be used to create a wide variety of phantoms and makes it an ideal candidate as a calibration and test material for the work in this thesis.

Recently, 3D printing has become of interest to the medical physics community for the application to phantom design. 3D printing is a form of additive manufacturing in which geometrical designs are used to construct physical models (Tofail et al., 2018). Through this layer-by-layer approach, complex and detailed structures are able to be created that would otherwise be impossible.

3D printing has been used in the past to create models of bone with cortical and trabecular porosity (Bose et al., 2013; Seitz et al., 2005; Tofail et al., 2018). The approach of the creation of these models all involves printing the bone material in a way that leaves spaces, to act as pores in the model. Unfortunately for the type of phantoms being created for bone lead XRF measurements, this is not a suitable technique as the material used for bone must have the ability to be doped with lead. The past work does however act as direct inspiration for the designs described later in this thesis, and we have created new phantoms using a combination of 3D printing techniques and plaster of Paris doping.

$^{109}\text{Cd}$  K XRF measurements can be considered to be the most successful application of the XRF technique *in vivo*. A history of bone lead XRF was described by Chettle & McNeill, (2019). Initial studies using XRF for bone lead measurements with  $^{57}\text{Co}$  were the first to show that lead does accumulate in the bone, and act as an endogenous source long after exposure (Christofferson et al., 1984; Craswell et al., 1984; Nilsson et al., 1991). These studies showed that the biological half-life of lead in bone was higher than previously thought, being present for decades past exposure and explained why individuals blood lead levels would remain elevated long after exposure. Through K XRF bone lead measurements, it has been shown that previous lead exposure increases the likelihood of high blood pressure in men and women (Gerr et al., 2002). It was also shown that women chronically exposed to lead will undergo menopause earlier than those not exposed (Popovic et al., 2005). Other associated issues with lead exposure include lower neurobehavioral scores in men, higher instances of Parkinson's disease and anti-social

behaviour in children (Needleman et al., 1996; Schwartz et al., 2005; Weisskopf et al., 2010). Notably, it was shown that men and women have different levels of endogenous exposure, and endogenous exposure may not be a linear relationship for women, which will be further discussed in section 1.7 (Behinaein et al., 2012; Popovic et al., 2005).

Of particular interest to this thesis are the bone lead surveys conducted in 1994 in Spokane, WA, by the University of Maryland and McMaster University in 1994. Through funding by the U.S. Agency for Toxic Substances and Disease Registry, two populations who had been exposed to lead from the Bunker Hill Smelter in northern Idaho were studied. First, a population of 108 women who were former smelter workers, and 99 age matched non-exposed women acting as a control group had bone lead measurements as part of a study of long-term health effects of occupational exposure. Second, 281 young adults who had been exposed to lead in early childhood and 287 age matched non-exposed young adults acting as a control group had bone lead measurements as part of a study to determine whether their childhood exposure had resulted in adverse effects as adults. Of these young adults, there were 145 exposed and 145 non-exposed young women. Some of the outcomes from these studies are described in later sections of this introduction.

### 1.7. Lead metabolism

After entering the body, lead behaves in a similar manner to alkaline earth metals, specifically calcium (Leggett, 1993). This similarity is seen in the way lead and calcium behave in bone. Lead and calcium have been shown to compete for the same position in

bone structures, in both trabecular and cortical bone (Hursh, 1973). Lead will replace calcium in the crystalline bone structure, creating similar patterns as what would be expected with calcium. The hormones responsible for the metabolism of calcium will also regulate lead if it has replaced calcium in the matrix. This equivalency to calcium process does break down when the concentration of lead in bone reaches higher levels (Anderson & Danylchuk, 1977), .

Lead enters the body through inhalation or ingestion but can also be absorbed through the skin depending on whether it is bonded to an organic compound. Lead then enters the bloodstream, where it can be distributed to a variety of locations in the body. However more than 90% of lead will end up in calcified areas of the body, such as bone (Barry, 1975; Wani et al., 2015). We see a biological half-life for lead in blood of 40 days, however in bone, the half-life is estimated around 30 years. This allows bone lead measurements to quantify long term accumulation of lead (Barry, 1975; Wani et al., 2015). As bone remodels, lead will be reintroduced to the blood, creating a cycle of Pb. If an individual has been exposed to lead in the past, but is currently not being exposed, the blood Pb and bone Pb lead levels can be correlated, as almost all blood pb is due to endogenous exposure.

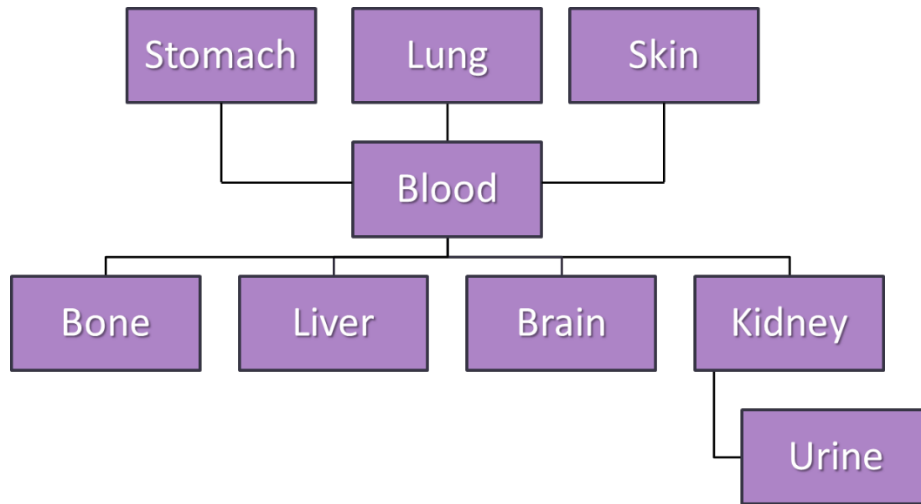


Figure 1.2 Biokinetic model of lead in the human body. Figure created by ©Fiona McNeill

Previously, the endogenous exposure rate of young men and women has been examined. A group of young adults was studied 20 years after they had been exposed to lead in childhood (Stokes et al., 1998). Through these previous studies, it was shown that young men and women do not release lead from bone back into the bloodstream at the same rate (Popovic et al., 2005). As seen in figure 1.3 and 1.4, the release rate of lead from bone is different from men and women. A linear fit best models the endogenous lead exposure for young men, however when we look at young women, it appears that a non-linear fit may better represent the data, with an increase in exposure as age increases.

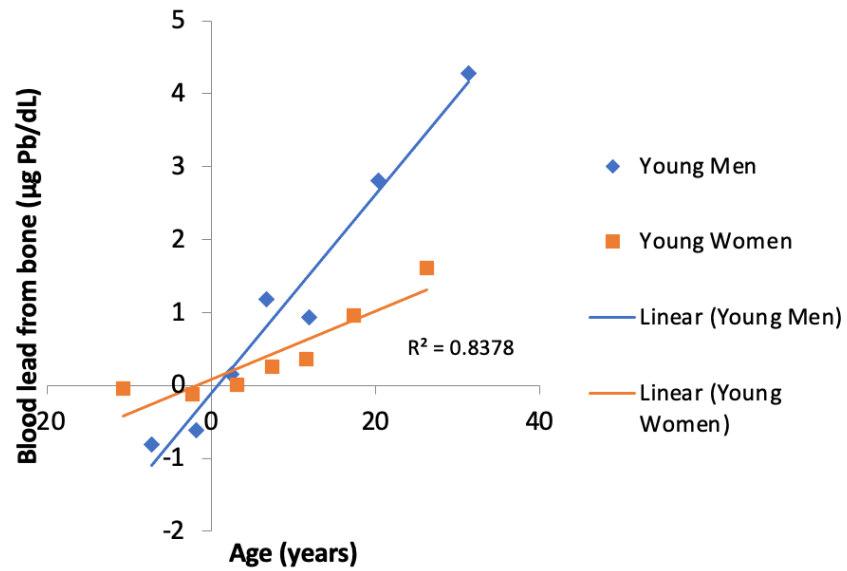


Figure 1.3 Endogenous exposure of lead versus age for young men and women. Figure created by ©Fiona McNeill

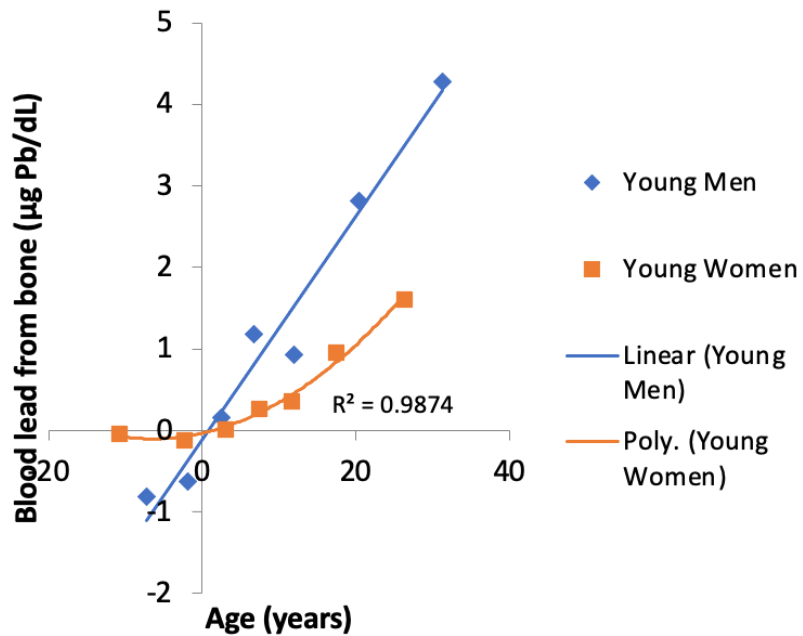


Figure 1.4. Endogenous exposure of lead versus age for young men and women. Figure created by ©Fiona McNeill

Another study involving former women smelter workers also found that young women (prior to menopause) do not have the same endogenous exposure rate for lead as men. However, it appears the release rate changes at menopause with postmenopausal women having similar levels when compared to men.

Table 1-1 Comparison of endogenous lead exposure rate for different groups (Popovic et al., 2005)

<b>Group</b>	<b>Release rate from bone</b>
Young women < 30 years	0.052
Premenopausal women 35 – 55 years	0.067
Postmenopausal Women 45 - 80 years	0.132
Young men	0.126

### 1.8. Bone metabolism

Endogenous lead exposure occurs because although sometimes thought to be static, bone is a dynamic organ, undergoing continuous remodelling. Bone mineral is made up of hydroxyapatite  $[(Ca)_{10}(PO_4)_6(OH)_2]$ .

Histologically, there are two forms of bone, trabecular and cortical. Trabecular bone typically makes up the inside of bones. It has a lower density and larger number of canals. Cortical bone is typically found on the outer surface of flat bones, or the shaft of long bones. It is denser, and in a more consistent structured form compared to trabecular bone. 80% of the bone mass found in our body is cortical bone, with the remaining 20% being trabecular (Morgan & Gerstenfeld, 2020). Cortical bone has channels formed throughout

its layers which allow blood vessels, lymphatics, nerves, and connective tissue to move through (Datta et al., 2008). These canals are also known as haversian systems.

Bone remodelled depends on several factors such as mechanical forces, bone cell turnover, hormones, cytokines and age (Datta et al., 2008). Bone metabolic unit (BMU) comprised of osteocytes, osteoclasts, and osteoblasts actively remodel bone based on mechanical stress and biochemical signals. Osteocytes will activate osteoclasts which then degrade the bone, which causes resorption. Osteoblasts will then synthesize bone mineral. Depending on the factors listed above, this process can cause bones to grow, remain the same, or decrease in volume.

As bone is remodelled, lead, following calcium, is released, or incorporated into bone. Changes in bone remodelling rates, for example at menopause, are thus also expected to result in changes in the rates of exchange of lead between different body compartments. If the level of lead exposure changes over time, the level of lead laid down in remodelled bone locations is expected to vary with the level of exposure.

### 1.9. Cortical Porosity

Although there are a variety of levels of porosity seen in cortical bone, when discussing cortical porosity, it is typically referring to the vascular porosity in the cortex (Cooper et al., 2016; Morgan & Gerstenfeld, 2020).

As discussed earlier, BMU's actively remodel bone, and in cortical bone these units create cone shaped cavities from the bones surface (Cooper et al., 2006). These cavities will then be filled by osteoblasts.

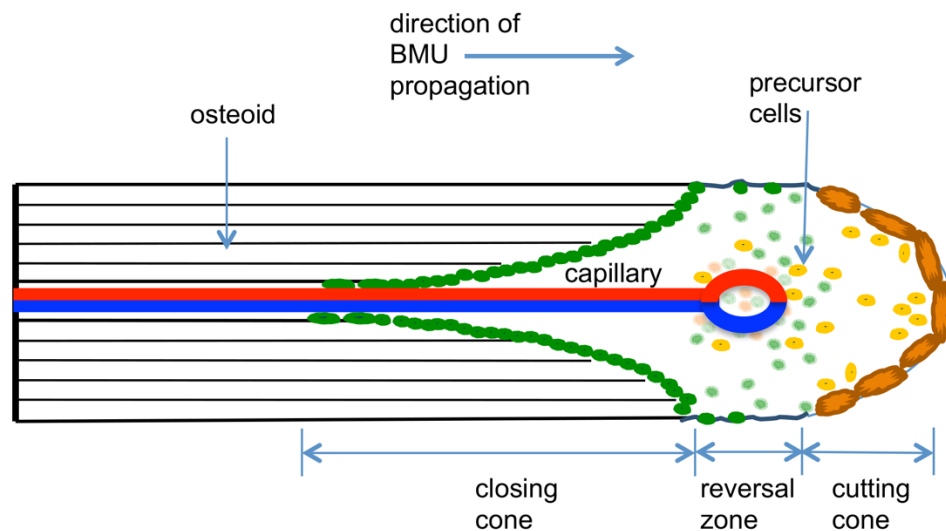


Figure 1.5 “Idealized structure of cortical BMU in longitudinal section, showing cutting cone, reversal zone and closing cone. (Smith et al., 2012)”

Smaller cavities can also be created within pre-existing surface cavities, resulting in haversian canals, within haversian canals. These canals have specific osteoclasts which differentiate from those seen in surface level canals (Cooper et al., 2016).

Micro-computed tomography, or micro-CT is currently the highest resolution form of imaging for cortical porosity, capable of depicting micron and nanometer levels of resolution (Cardoso et al., 2013). These devices operate on the same principles as a typical CT machine but are optimized for higher resolutions. Currently Micro-CT is limited to ex-vivo measurements and animal studies, as the exposure levels needed to produce images of individual pores is above acceptable levels of radiation exposure for individuals.

Synchrotron radiation micro XRF (SR  $\mu$ -XRF) is a technique based on the same principles as the XRF but utilizes radiation from a synchrotron. This technique has been used to map out trace element distributions in bone (Pemmer et al., 2013). As seen in the figure below, cortical porosity can create areas of bone absent of trace elements found distributed throughout the rest of the bone (Pemmer et al., 2013).

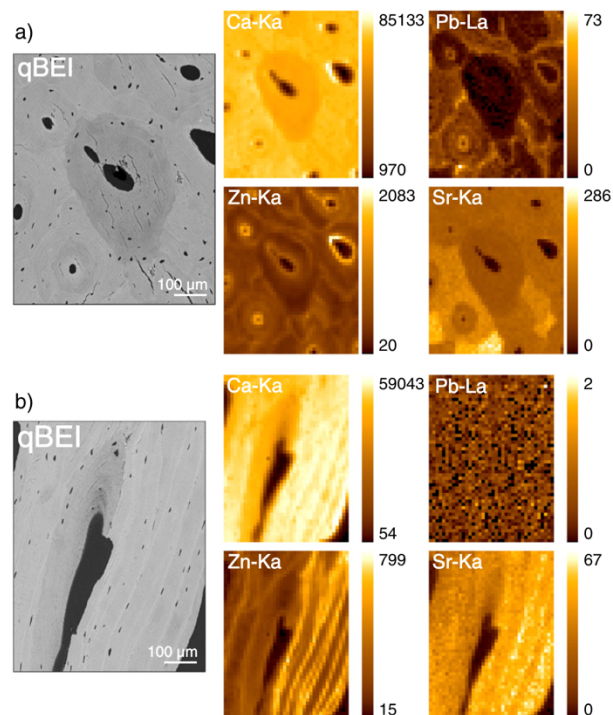


Figure 1.6 From “Spatial distribution of the trace elements zinc, strontium and lead in human bone tissue”, p. 188, by (Pemmer et al., 2013). “Examples of qBEI images with corresponding SR  $\mu$ -XRF element maps of Ca, Zn, Pb, Sr: (a) osteonal bone region of the human femoral neck. The color-coded X-ray intensities are normalized to counts per second (cps), 100 mA Ring current and are scaled from minimum to maximum within each individual map. qBEI images show younger bone packets (less mineralized) as darker, and older bone packets (more mineralized) as brighter gray levels. Sample (b) exhibiting multiple parallel cement lines.”

While it does not have the spatial resolution of micro-CT or synchrotron micro-CT, the technique of HR- pQCT (high resolution peripheral quantitative CT) can be used to study cortical porosity in vivo (van den Bergh et al., 2021). It has a spatial resolution in the range of 100  $\mu\text{m}$  (Cooper et al., 2003) which is close to the resolution of individual trabeculae (Nishiyama & Shane, 2013; Vilayphiou et al., 2016). Over the last fifteen years, the technique has allowed better study of the bone architecture of the tibia.  $^{109}\text{Cd}$  K XRF bone lead measurements have assumed that bone remodelling in the tibia was more limited than other bones such as the calcaneus and the limited remodelling would result in the bone architecture remaining essentially the same. However, HR-pQCT has shown these assumptions may not be true.

The level of cortical porosity has been shown to depend on age and gender. Women's bones have more cortical porosity than men (Burghardt et al., 2010). The increase in cortical porosity in the tibia of women has been found to increase exponentially from the age of 25 (Vilayphiou et al., 2016). In addition, studies comparing young men and women found that tibia cortical porosity changed significantly between the ages of 16 and 29 in women but not in men (Burt et al., 2014).

It is conceivable that cortical porosity could be linked to endogenous exposure, as higher porosity would mean a higher bone surface area at which exchange of lead could take place. The non-linearities observed in endogenous release rates of lead from bone in women, but not in men, seem to map onto the non-linear cortical porosity changes observed in women.

This is maybe a physiological explanation for the observed non-linearity. However, an alternative explanation that could not be ruled out at the start of this work, is that the changes in cortical porosity create a measurement artifact that makes the relationship between blood and measured bone lead level only appear non-linear. This possibility is what this thesis aims to explore.

## 2. Methods of Experimental Porous Bone Phantom

### 2.1. Creating a 3D printable porous bone model

In medical physics, a phantom is a realistic, controllable model that acts as a substitute for a specific organ or tissue. Ideally, a phantom would be created with the exact chemical and physical composition of the organ, and its geometry, including the size, shape and density. For the specific purposes of this XRF bone lead system for measurements of lead in tibia, a phantom would encompass the geometrical and compositional properties of a tibia and surrounding tissue. When creating a phantom for XRF measurements, having phantoms with known elemental mass quantities that match humans, and that can be doped with specific quantities of lead, allow for them to be used to calibrate the system. For the case of XRF measurements, it is important that the materials in the phantom behave similarly to human tissue when considering photo-atomic interactions such as coherent scattering, incoherent scattering, photoelectric interactions and pair production. Depending on the model, creating a ‘perfect’ phantom can be impractical or near impossible. Cost,

reproducibility, and manipulability all need to be considered when deciding where to compromise.

For forty years, bone lead XRF phantoms have been created using plaster of Paris ( $CaSO_4 \cdot \frac{1}{2}H_2O$ ) which is mixed with water to create  $CaSO_4 \cdot 2H_2O$  to act as a surrogate to bone. Plaster of Paris differentiates most notably from hydroxyapatite ( $Ca_{10}(PO_4)_6(OH)_2$ ), the crystalline material in bone, with its calcium sulfur content compared to calcium phosphate. This difference is usually accounted for in in-vivo bone lead studies with the application of a correction factor when comparing the bone and phantoms, or when using phantoms to calculate in vivo bone lead concentrations, as there is a difference in the coherent scattering properties of these two materials.

As discussed in the introduction, in the past bones have been modelled in phantoms as being homogenous in composition, lead distribution and density with the assumption that these factors did not matter because of the normalization of the lead x-ray signal to the coherent signal. The objective of my work is to create a model that more accurately models cortical porosity and allows the effect of lead distribution to be studied.

As also discussed in the introduction, cortical porosity typically appears in perpendicular channels to the surface of the bone. The typical diameter of cortical porosity in real human's ranges from 50-300 microns (Vogl et al., 2017). With currently available technology we are able to 3-D print structures at the upper limit at 300 microns.

3-D porous bones have been printed by various researchers with materials such as PLA, polylactic acid/  $\beta$ -tricalcium phosphate and tetra-calcium phosphate. However, all these models were printing the bone structure, and this is not possible for in vivo elemental analysis bone phantoms as we must be able to dope the material with various trace elements, in this specific instance, lead (Bose et al., 2013). However, we used these previous bone phantom designs as inspiration and created a ‘negative’ model that represents the soft-tissue porous structures in bone. The gaps around the ‘soft tissue’ can then be filled with a bone-mimicking material.

In our phantom, polylactic acid ( $C_3H_4O_2$ ) or PLA was used as a soft tissue equivalent and to represent the porous structures of bone. This material was chosen for its high resolution in 3D printing, as well as its physical properties being a reasonable tissue equivalent, particularly with regard to x-ray scattering and attenuation.

Using Autodesk Inventor, a three-dimensional model was created in the form of a lattice. The final thickness and diameter of the lattice was limited based on the printer’s capabilities as well as structural limitations. These capabilities and limitations are discussed more fully in the following section. The final phantom design created was a 33mm x 33mm x 33mm hollow cube printed with PLA, with a 2mm outer wall thickness. A PLA lattice structure occupying 11% of the volume in a uniform grid is placed inside the hollow cube. The lattice consists of  $1.2\text{mm}^3$  hollow cubic areas, these areas are formed by a wire structure

with a diameter of 300 microns. This pattern is consistently repeated through the structure, with the wire structure occupying a total volume of 11%. This design allows for these hollow areas to be filled with a liquid suspension of plaster of Paris.

To reach the final design, the limitations of 3-D printing readily available within the lab were explored by creating models with varying thicknesses of ‘soft tissue’ lattice. Sizes of the lattice ‘wire’ ranged from 50 microns to 1000 microns. Only the 1000-micron model was found to be viable when printed due to structural issues. As shown in Figure 2.1, smaller sizes were found not to be possible, so a third-party printing company was enlisted to attempt to achieve results that better approximated ‘true physiology’. Using this third-party printing company, the smallest diameter possible to print while maintaining the integrity of the lattice structure was found to be 300 microns. This printed lattice is shown in Figure 2.2.

In addition to printing the lattice structure, a hollow cube was printed to place the lattice inside. This cube acts as a barrier to keep the plaster of Paris contained, as well as simulating a small overlay of soft tissue over bone. The cube is shown in Figure 2.3



Figure 2.1 Unsuccessfully 3D printed lattice structure.

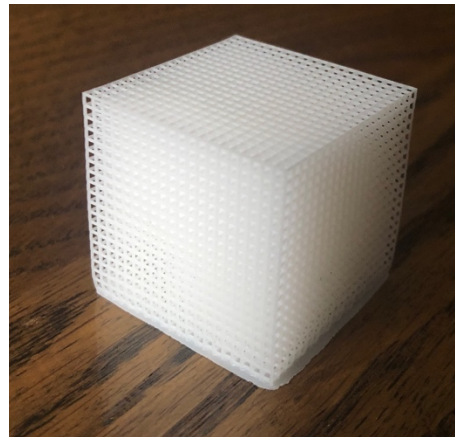


Figure 2.2 Successfully 3D printed Lattice structure



Figure 2.3 3D printed cube for housing lattice structure.

## 2.2. Filling a 3D printable porous bone model

The bone in the phantoms was modelled using hydrated plaster of Paris ( $\text{CaSO}_4 \cdot 2\text{H}_2\text{O}$ ), the material that has been used for K XRF in vivo bone lead measurement calibration for several decades. While this is not perfectly equivalent to bone, it has the advantages of being pourable and low cost. It is also easy to dope plaster of Paris with various concentrations of lead for calibration purposes. As plaster of Paris is not an ideal model for bone, a correction factor is employed to account for the differences in x-ray scattering. To re-iterate the phantom design, polylactic acid ( $\text{C}_3\text{H}_4\text{O}_2$ ) or PLA was used as a soft tissue equivalent and to represent the porous structures of bone. Lead acetate mixed with water in varying concentrations was added to the plaster of Paris to lead-dope the bone material. The lead-doped plaster of Paris was then poured into the gaps in the PLA structure to model the bone.

Table 2-1 Material weights for lead plaster of Paris phantoms.

Parts per Million(ppm)	Plaster (powder) (grams)	Water – lead (grams)	Lead acetate (micro-grams)
16.25	18.98	18.59	380
24.38	18.98	18.41	569
40.63	18.98	19.03	949
48.75	18.98	18.98	1139
56.86	18.98	17.65	1328
81.25	18.98	17.08	1898

In order to fill the phantoms, powdered plaster of Paris and a pre-mixed solution of lead acetate and water were mixed directly inside the hollow PLA cube. Immediately after mixing, the PLA lattice cube was slowly lowered into the liquid plaster.

In previous studies creating bone phantoms with plaster of Paris, the amount of water used has been kept to the minimum required, creating a denser final ‘bone’ structure. Due to the fine structures of the 3-D lattice placed into the plaster of Paris suspension in the phantoms, a larger amount of water was required to allow the solution to flow evenly through the gaps in the phantom ‘bone’ lattice. Mixtures of powdered plaster and water were experimented with to determine the current ratio for this scenario. Mixtures between 1:2 water to plaster and 3:1 water to plaster were examined. Mixtures of 1:2 and 1:1 water and plaster had too high a viscosity to flow through the channels in the phantom evenly before drying. It was found that at ratios greater than 2:1 water to plaster, although having a suitable viscosity initially, the plaster of Paris suspension began to separate under gravity, resulting in a greater amount of plaster at the bottom of the phantom. For this reason, the final suspension consisted of a 2:1 mixture of water to plaster based on weight. Due to this increase in water, and the fact that the phantoms are surrounded by the outer box, these phantoms required a long time to dry, they were left for 14 days to completely dry before being sealed. Figure 2.4 shows a filled drying lattice phantom. Once dry, phantoms were scrubbed clean on the outside and sealed with plastic wrap and tape to limit any contamination.



Figure 2.4 Cross section of filled lattice phantom.

### 2.3. Measuring and analyzing bone lead phantoms

The phantoms were measured using the  $^{109}\text{Cd}$  K XRF bone lead XRF system at McMaster (Nie et al., 2006b). This system utilizes four 16mm diameter, 10 mm thick high purity germanium (HpGe) detectors in a clover leaf shape. The  $^{109}\text{Cd}$  source is positioned in front of the detectors. The source is mounted inside a tungsten collimator, with a 0.5 mm copper filter over the opening.  $^{109}\text{Cd}$  decays by electron capture and emits an 88.035 keV  $\gamma$ -ray in 4% of decays as shown in Figure 2.5. The decay is down through excited states of silver and thus the source emits silver x-rays at 22 and 24 keV. The copper filter thus reduces the silver x-ray emission by 71% while only reducing the  $\gamma$ -ray emission by 3%. The  $^{109}\text{Cd}$  had a nominal activity of 5GBq in June 2020. However, the source is plated onto a silver plug and encapsulated in titanium, so this 5 GBq value means the emission of 88 keV  $\gamma$ -rays at the source surface is equivalent to the emission of 88 keV  $\gamma$ -rays from a bare source.

Differential attenuation means that the surface emission of silver x-rays is less than would be expected from a bare source. Insertion of the source inside the tungsten collimator means that the detectors cannot see direct source emission.

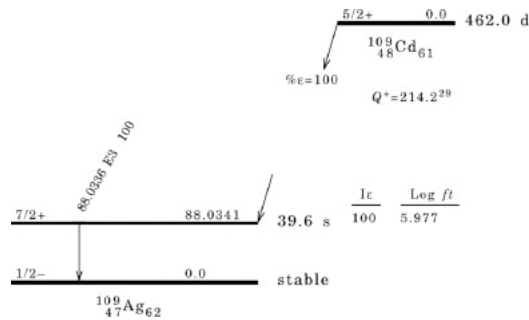


Figure 2.5  $^{109}\text{Cd}$  decay scheme (Xiaolong et al., 2010).

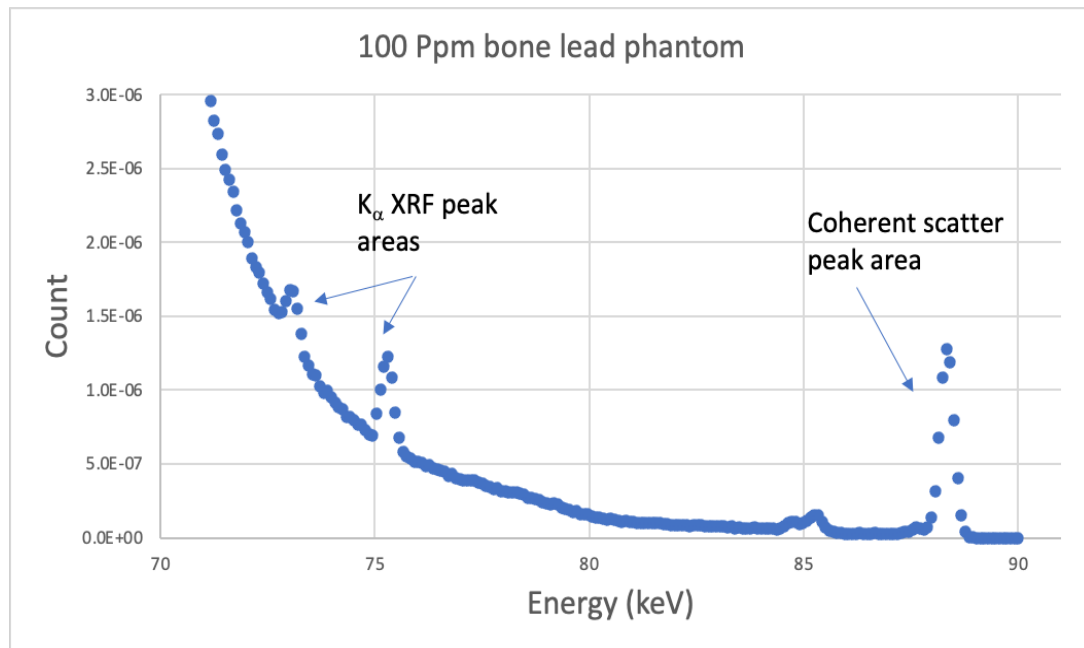


Figure 2.6 Sample detector spectrum from  $^{109}\text{Cd}$  bone lead XRF system

The x-ray and coherent peak intensities were extracted from the measured phantom spectra by fitting a mathematical model to the spectra. Spectral analysis was completed using

Origin © software. The coherent scatter peak area from the scatter of the 88.035 keV  $\gamma$ -ray from  $^{109}\text{Cd}$  is analyzed using a Gaussian function with a second Gaussian function used to model the close neighbouring Pb  $\text{K}\beta_2$  x-ray peak at 87.23 KeV.

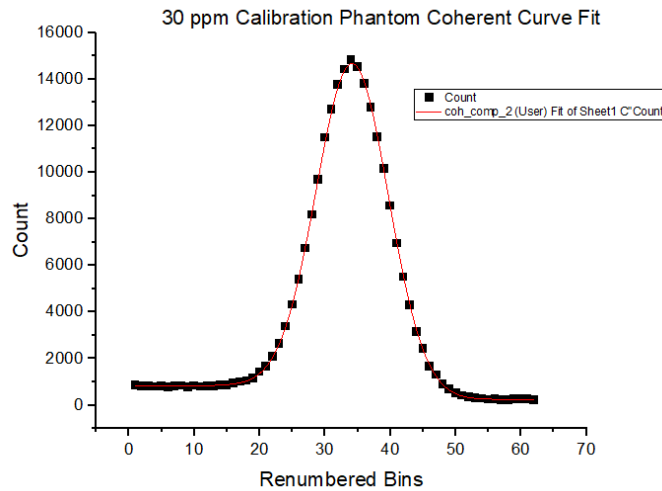


Figure 2.7 Curve fitting of Coherent area of spectrum using Origin © software.

In addition, the model includes an offset to model a linear background signal plus a complimentary error function to model the ‘step’ that appears in the spectrum under the coherent peak which is attributed to incomplete charge collection in the detector. A number of variables are therefore determined by the fit including: variables to represent the amplitude of the gaussian modelling the coherent peak; the amplitude of the Pb  $\text{K}\beta_2$  x-ray peak; the coherent peak position; the width of the coherent peak. To reduce the number of fitting parameters, the position of the Pb  $\text{K}\beta_2$  x-ray is tied to the position of the coherent

peak and the width of the Pb  $K_{\beta 2}$  x-ray is assumed to be the same as the coherent peak width.

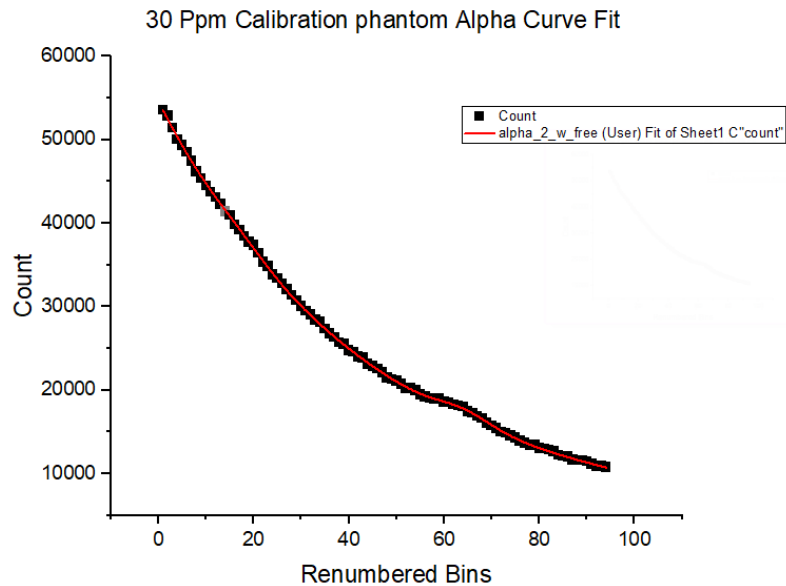


Figure 2.8 Curve fitting of  $K_{\alpha 1}$  and  $K_{\alpha 2}$  area of spectrum using Origin © software.

The area of the spectrum corresponding to the Pb  $K_{\alpha 1}$  and  $K_{\alpha 2}$  x-ray peaks was fit using a polynomial to represent the background and used two Gaussian functions to represent each of the x-ray peaks. The position and amplitude of the Pb  $K_{\alpha 1}$  and  $K_{\alpha 2}$  x-ray peaks were tied together to reduce fitting parameters and the peaks widths were modelled using the coherent peak width. The variables determined by the fit are the parameters for the polynomial background and the position and amplitudes of the Pb  $K_{\alpha 1}$  and  $K_{\alpha 2}$  x-ray peaks.

As described in the thesis introduction chapter, the Pb  $K_{\alpha 1}$  x-ray area is then normalized to the coherent area to create calibration lines, as this makes a robust measurement that has been considered for four decades to be independent of bone shape, size, mass or tissue

overlay thickness. To construct a calibration line, the  $K_{\alpha 1}$ /coherent ratio is plotted against the known concentration of lead in the phantoms. This calibration line can be used to quantify the concentration of lead within a person or unknown sample by comparing the signal from the person or unknown sample with the calibration line. The calibration line variables are determined using a linear regression of the observed Pb  $K_{\alpha 1}$  x-ray area/coherent area versus the known concentration of lead.

### 3. Results and Discussion of Porous Bone Phantom

#### 3.1. Cylindrical tibia phantom measurements and calibration line

For the past four decades, lead doped plaster of Paris phantoms have been used to create a calibration line for in vivo K XRF bone lead measurements. In our laboratory, a pre-existing set of these phantoms were created in plastic cylindrical containers, to contain the plaster of Paris and keep it free from contamination. The high-density polyethylene (HDPE) container is wipeable and acts as a thin layer of soft tissue. The mass attenuation coefficient for HDPE and soft tissue are similar at the energies used in the  $^{109}\text{Cd}$  bone lead system.

Table 3-1 The mass attenuation coefficient and x-ray interaction cross-sections ( $\text{cm}^2/\text{g}$ ) for soft tissue and HPDE at significant x ray energies for lead K-XRF measurements (ICRU, 1989).

	Total attenuation		Incoherent scatter		Coherent scatter		Photoelectric absorption	
	Soft tissue	HPDE	Soft tissue	HPDE	Soft tissue	HPDE	Soft tissue	HPDE
88.035 keV	0.177	0.178	0.165	0.172	0.00654	0.00412	0.00386	0.00135
74.969 keV	0.189	0.186	0.170	0.178	0.00885	0.00560	0.00656	0.00231
65 keV	0.199	0.193	0.174	0.182	0.0115	0.00733	0.0195	0.00372

For the purposes of this thesis, these pre-existing phantoms will be referred to as “cylindrical” phantoms. As seen in figure 3.1, when looking at the calibration line obtained from the cylindrical phantoms in one detector of the four in the system, we see a strong

correlation between the ratio Pb  $K_{\alpha 1}$  peak area/coherent peak area and Pb concentration ( $p < 0.001$ ), with an R-Squared of  $0.9977 \pm 0.0048$ . Table 3.2 shows the comparison the slopes obtained from the four detectors in this work, with the slopes of the same phantoms and a similar detector system in a publication from our laboratory in 2011. There are two almost identical clover leaf systems in the laboratory. We cannot conclude that we are comparing results from the same detector over time. However, the determined slopes are consistent with previously published values.

Table 3-2 Pb  $K_{\alpha 1}$  peak area/coherent peak area from this work and Behinaein et al., 2011.

Slopes in this work	Slopes in Behinaein et al., 2011
$0.00277 \pm 0.00003$	$0.00298 \pm 0.00002$
$0.00278 \pm 0.00003$	$0.00280 \pm 0.00004$
$0.00282 \pm 0.00006$	$0.00302 \pm 0.00003$
$0.00273 \pm 0.00003$	$0.00306 \pm 0.00002$

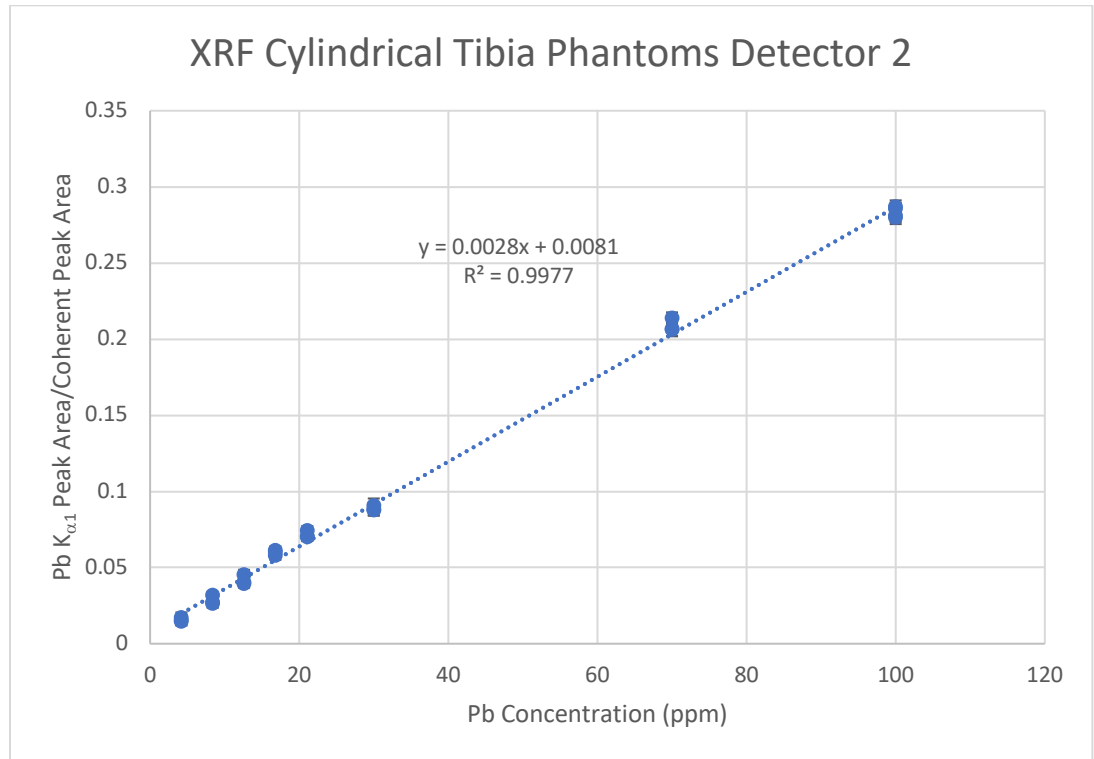


Figure 3.1 Pb concentration vs. Pb K<sub>α1</sub> peak area/coherent peak area for cylindrical phantoms

When we consider all the detectors in the system, taking the average of the Pb K<sub>α1</sub> peak area/coherent peak area for each measurement, we see a strong correlation between the ratio Pb K<sub>α1</sub> peak area/coherent peak area and Pb concentration ( $p < 0.001$ ) for  $n = 25$ . The linear regression shows an R-Squared value of  $0.9965 \pm 0.0058$ , with a similar slope and intercept to the single detector previously discussed above. We observe a slope of  $0.0028 \pm 0.00003$ , with a y-intercept of  $0.0045 \pm 0.0017$ . This intercept is significantly different than zero ( $P = 0.012$ ) for  $n = 25$  and suggests an intercept of  $1.6 \mu\text{g Pb per g of plaster of Paris}$ . This level of offset is reasonable and is most likely some contamination in the plaster of Paris.

Figures 3.1 and 3.2 together show that all the system's detectors are functioning in agreement to one other and compare well to prior data. These measurements are thus be considered our 'baseline' for comparison with the results from other phantom designs discussed in the following sections.

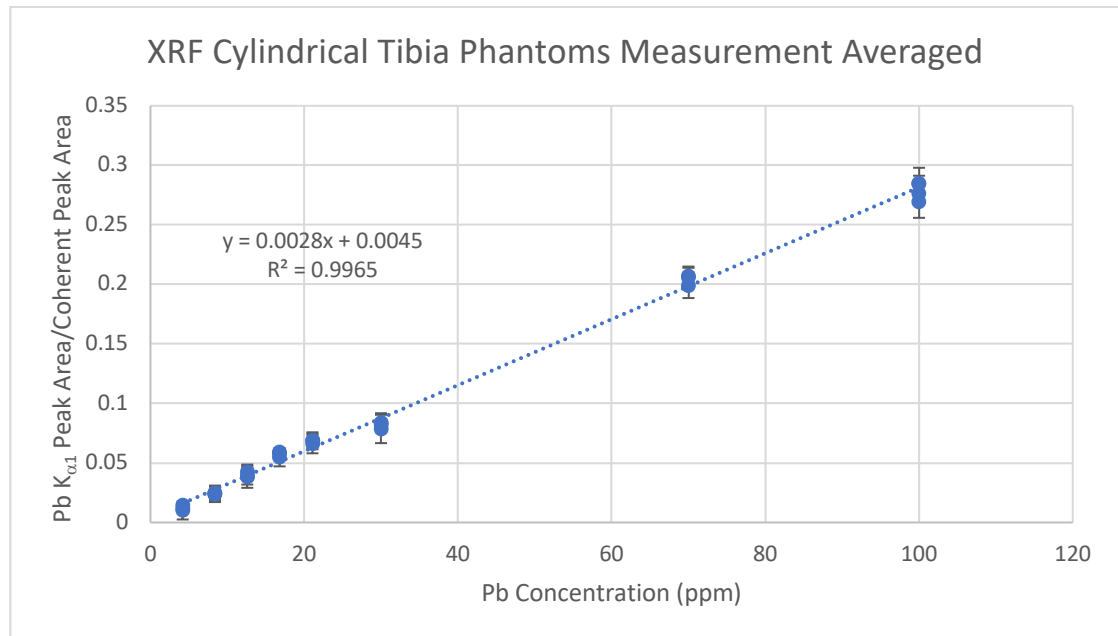


Figure 3.2 Pb concentration vs. average Pb K<sub>α1</sub> peak area/coherent peak area for cylindrical phantoms.

### 3.2. Lattice tibia phantom measurements and calibration line

As discussed in section 2.1 of the methods, new phantoms were created with a lattice design structure to emulate the cortical porosity found in human bones. These phantoms will be referred to as lattice phantoms for the purposes of this thesis.

Each lattice phantom was measured for 40 minutes, and spectra were collected from all 4 HpGe detectors separately. Phantom measurements were repeated 4 times. Spectra were fitted with a mathematical model using the technique described in section 2.3 of the methods to extract peak areas. The average reduced Chi-Squared value for the coherent area fit from multiple spectra measurements was 1.37 while the result for the K Alpha x-ray peak area was 1.12. These Chi-squared values indicate that the peak fitting algorithm can be considered acceptable. The four spectra from the four detectors were fit independently from each other, then the ratio of the alpha peak area to coherent peak area was averaged for each measurement.

Lattice phantoms were created with concentrations of Pb between 16 and 50 ppm ( $\mu\text{g Pb per g of plaster of Paris}$ ). Figure 3.3. shows the regression of the ratio of the Pb  $K_{\alpha 1}$  area/coherent peak area versus Pb concentration. This data shows a R-squared value of 0.897 for  $n=18$ . There is more uncertainty in these measurements because the lattice phantoms are smaller than the cylindrical phantoms. When comparing to our cylindrical phantom calibration line slope ( $0.0028 \pm 0.00003$ ) and the slope of the lattice phantoms ( $0.0030 \pm 0.00022$ ), we can see there is no significant statistical difference ( $p= 0.31$ ) between the slopes for  $n = 42$  measurements.

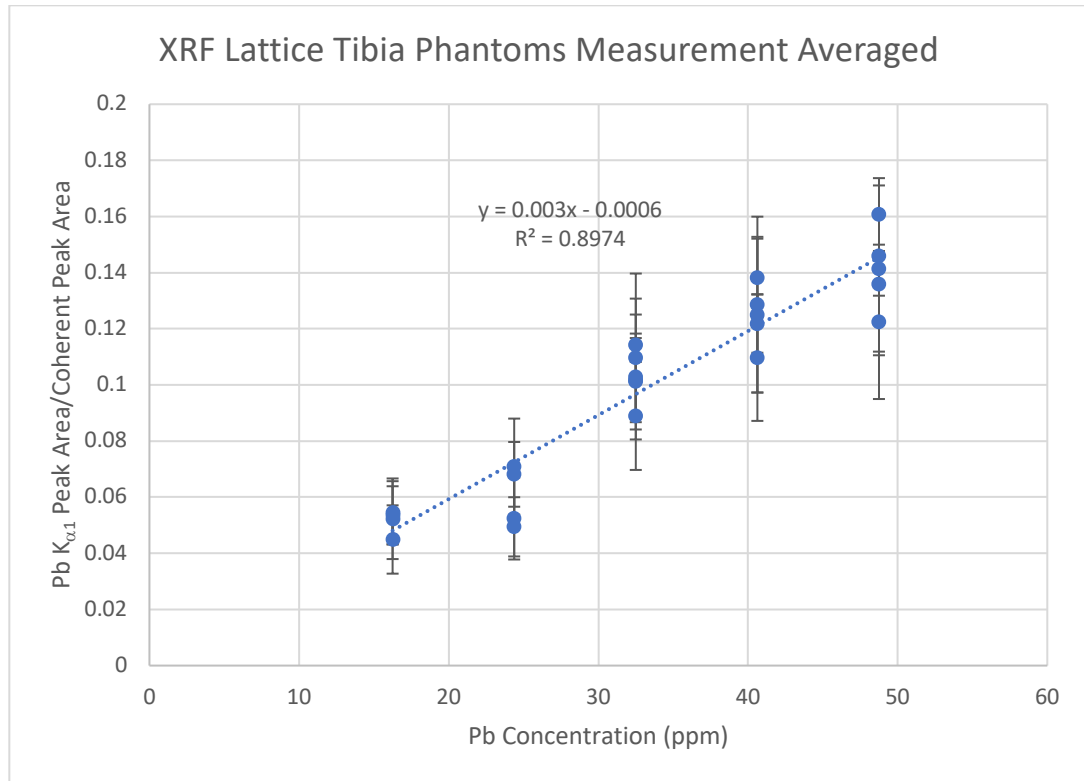


Figure 3.3 Pb concentration vs. Pb K<sub>α1</sub> peak area/coherent peak area for lattice phantom

The data presented above were phantoms from a second batch of lattice phantoms. This newer batch was created using a more refined technique that involved mixing all the plaster and water inside the cube that the lattice would then sit inside. This improved technique allowed for more consistent filling of the phantoms. Figure 3.4. below shows the data from these 5 phantoms compared with results from phantoms of the same concentration created in the first batch plus a 100-ppm phantom created in the first batch. We find that the phantoms agree when we look at the average value for each concentration measurements, but there is a significantly greater variation around the average value from the original batch. We see a small difference in slope of 0.0001, from a regression line with a R-Squared

of  $0.7801 \pm 0.040$  for  $n=21$  measurements. However, the difference between the slope of the curve in figure 3.4 and the baseline cylindrical phantom is not statistically significant ( $p=0.21$ ) for  $n=51$  measurements. As discussed, we see a larger standard deviation for the phantoms created in the first batch. The consistently lower standard deviation from the second batch shows the effectiveness of this improved technique. We deduce that there were increased losses in total plaster content in the phantoms from the first batch, and better mixing in the second batch led to a decrease in heterogeneity (or rather increase in homogeneity). These factors reduced the variation between measurements.

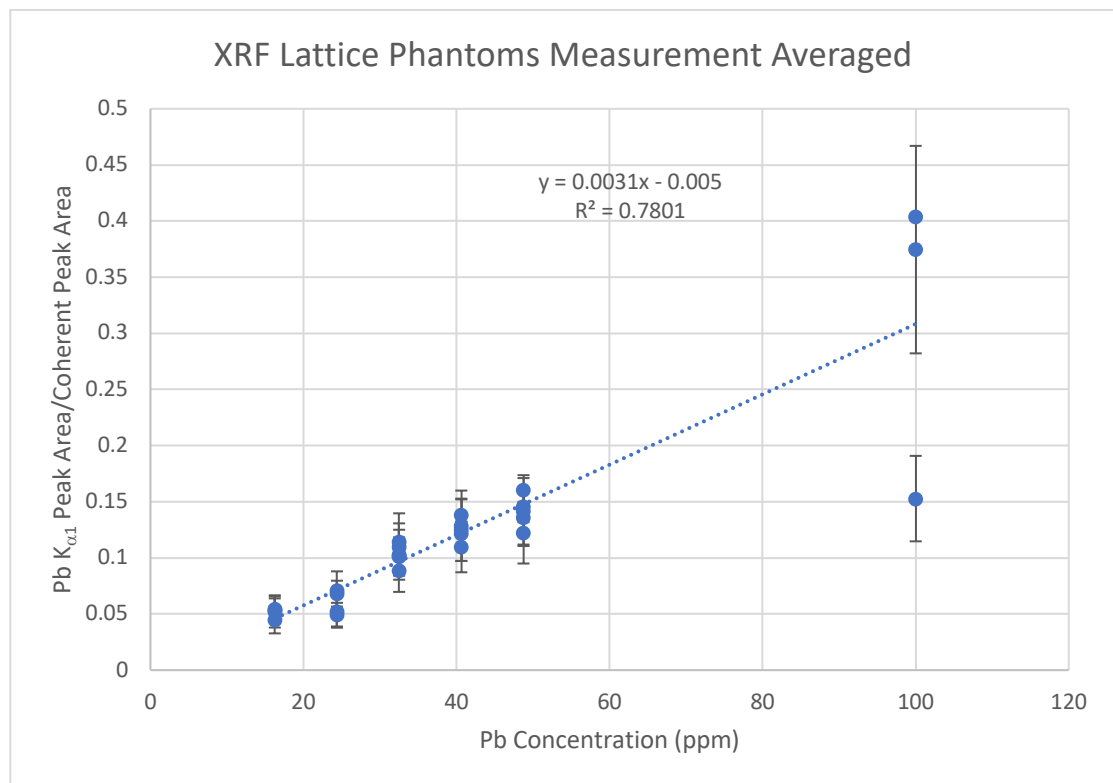


Figure 3.4 Pb concentration vs. Pb K<sub>α1</sub> peak area/coherent peak area for lattice phantom.

Calibration lines were created from the measurements from the four detectors for the lattice phantoms measurements in the same way that data from the cylindrical phantoms was

combined. Regression of the ratio of the Pb  $K_{\alpha 1}$  area/coherent peak area versus Pb concentration resulted in a R-squared value of  $0.964 \pm 0.008$  for  $n=5$  data points. When comparing the slope of the regression to our cylindrical phantom calibration slope, we can see there is no statistically significant difference ( $p=0.17$ ) for  $n=30$  data points.

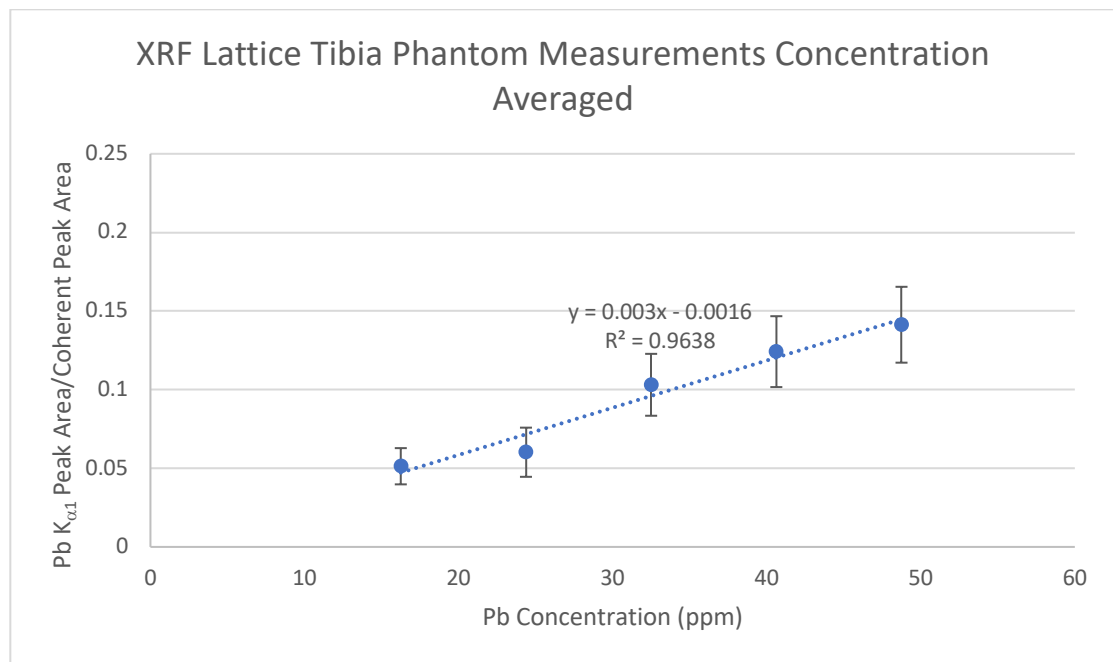


Figure 3.5 Pb concentration vs Pb  $K_{\alpha 1}$  peak area/coherent peak area for lattice phantoms

A regression line was created from all lattice phantoms in both batch 1 and 2 as seen in figure 3.6. below. This calibration line includes the 100-ppm lattice phantom from batch 1, although the standard deviation of the average of this concentration is significantly higher than other concentrations (42% for 100 ppm vs. 22% other concentrations). However, the average value of multiple measurements follows the expected slope of our calibration line. The regression of this calibration line of both batch 1 and batch 2 has a R-Squared value of  $0.9938 \pm 0.00011$ , with an X intercept of  $-0.0060 \pm 0.0060$ . The X intercept is not

statistically different than zero ( $p= 0.37$ ) for  $n=6$  data points. While the lattice phantoms are smaller than the cylindrical phantoms and have a lower density of the plaster of Paris because of the increased water used in mixing, the cylindrical phantoms and the lattice phantoms do not behave differently. The lattice, and by extension, the soft tissue of cortical porosity, does not perturb the accuracy of bone lead measurements if the lead is homogeneously distributed. The porosity will, however, increase the measurement uncertainty because of the lower mass of bone.

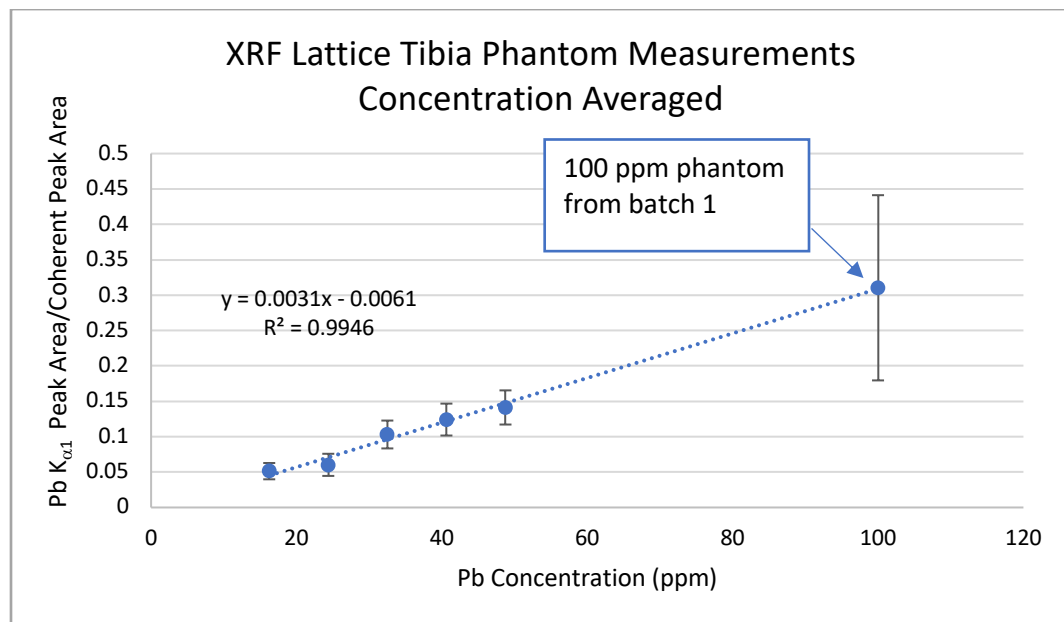


Figure 3.6 Pb concentration vs Pb K<sub>α1</sub> peak area/coherent peak area for lattice phantoms from batch 1 and 2

## 4. Methods of Monte Carlo Simulations of Porous Bone Phantom

### 4.1. Recreating models in MCNP

A model of the Pb K XRF bone lead measurement system was created in the Monte Carlo N-Particle transport code (MCNP). The version used for all simulations was MCNP 6.2

All physics parameters were set to default in the MCNP input file. This includes:

- Doppler broadening being set to on.
- Coherent scattering being set to on
- Generation of electrons from photons set to on.
- Photonuclear production being set to off.

F8 tallies were used to represent the energy distribution of a pulse created in a detector (Werner, 2018). The pulse information is stored in bins based on energy. MCNP automatically adjusts the information stored in these bins to be the count per  $\gamma$ -ray emission from the source. Since the silver x-rays emitted by the  $^{109}\text{Cd}$  source are filtered out experimentally, only the 88 keV  $\gamma$ -rays from  $^{109}\text{Cd}$  were modelled in MCNP.

The detector system dimensions were modelled based on the real system's dimensions: this included, for example, detector diameter, depth, source and phantom position. The simulation geometry is shown in Figure 4.1. To model system materials, the .12p data library is called for the phantom materials for a more detailed and accurate coherent scatter data (Hughes, 2014).

The source was initially modelled as an 88.035 keV x ray source since  $^{109}\text{Cd}$  has an  $\gamma$ -ray energy of 88.035 keV, just above the k-edge of lead which is at 88.035 as tabulated by both NIST (M.J. Berger et al., 2010) as well as the more recent ENDF data bases (which are not currently available in MCNP). However, after running the simulation with various lead concentrations, it was noted that no lead  $K_{\alpha}$  and  $K_{\beta}$  x-ray peaks were visible in the detector spectrum. Simulations were then run with increasing source energies to see if there was an energy binning effect or if the K-edge stored in the MCNP libraries was incorrect. When the source energy was set at or above 88.3 keV in the MCNP model, the missing Pb  $K_{\alpha}$  and  $K_{\beta}$  x-ray peaks appeared in the simulation. Investigation into the ENDF database revealed that the current library that MCNP calls with the .12p protocol (ENDF/B-VI.8, 2001), has the K-edge incorrectly listed at 88.29 KeV. This has since been updated in more recent x-ray interaction databases to match what is seen experimentally and tabulated in other sources, such as NIST, as 88.035 keV. However, those newer data bases do not have the required coherent scatter models and in order to more accurately model the coherent scattering in the system, which is an essential part of the  $^{109}\text{Cd}$  K XRF bone lead measurement technique, it was still necessary to use the library called by the .12p protocol. Due to the Pb K x-ray absorption edge discrepancy in the MCNP tables, the energy of the source was increased to 88.3 keV within the code to allow these Pb k x-ray shell interactions to be observed. This, of course, makes the assumption that a 265 eV  $\gamma$ -ray energy difference can be considered insignificant.

Simulations were run with for approximately 6 billion particles to reach a level uncertainty of 0.15 or below for each bin in the f8 tallies.

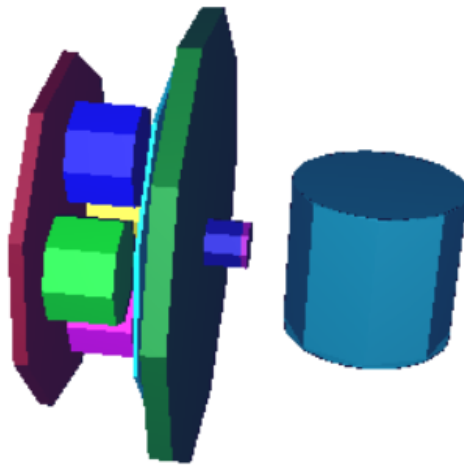


Figure 4.1 XRF system replicated in MCNP with a simple cylindrical bone lead phantom.

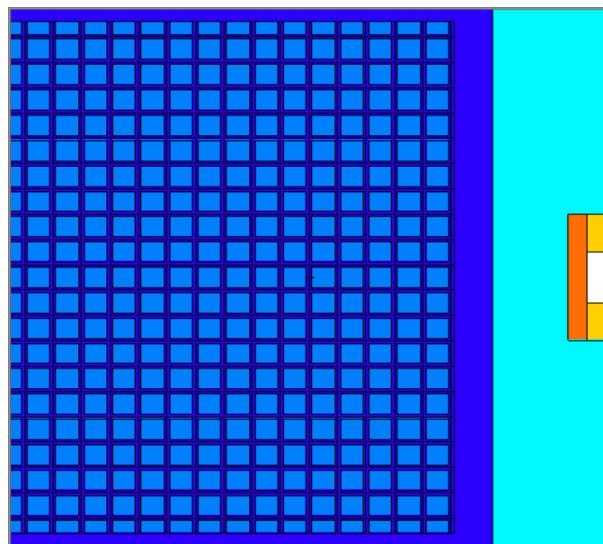


Figure 4.2 2-D view of lattice phantom in MCNP

To create the lattice phantom design, the lattice card in MCNP was employed. This card can be used to define an array of previously defined structures. As discussed above, the lattice phantom design is constructed of a repeating pattern of wire soft tissue structures, which is then filled with plaster. To create a repeating pattern out of this design, the structure can be imagined as a cube of soft tissue. Passing all the way through this cube in the x,y and z plane is a channel of plaster. This single cube is defined in MCNP in a separate “universe” than the detector system. Using the “fill” and “lat” card in MCNP, this simple structure was repeated to create the design seen in figure 4.2., matching the dimensions of the structure created previously using a 3D printer.

In addition to modelling the phantoms constructed for this study, simulations were run of phantoms which match the shape and design of the current set of in vivo bone lead measurement calibration phantoms. There is an extensive historical database of measurements using these phantoms and they thus serve as a well established and well-understood set of baseline measurements for comparison. These phantoms are cylindrical plastic containers filled with plaster of Paris. The phantom dimensions are 25mm radius, 70mm height, with a 2mm thickness. The phantoms have concentrations of lead varying from 4 to 100 ppm.

Simulations were run with lead concentrations between 0 and 100 ppm to create a calibration line. These calibration lines of the well-described phantoms were used for comparison with the calibration lines from the new lattice phantoms. Similar to the

experimentally measured phantoms, the analysis of the spectrum acquired from the detectors was completed using Origin © software using the same fitting functions for the coherent and  $K\alpha$  peaks with, however, altered initial parameters. Alpha/coherent ratios from the simulation were then plotted against their known concentrations to generate a calibration line.

#### 4.2. Testing the effect of bone lead distributions in MCNP

Following the creation of the lattice bone phantom and to further test how the distribution of bone and lead may affect XRF measurements, more phantoms were created in MCNP that could not be created experimentally in the lab. Phantoms were created within the model with increasingly larger variations in the distribution of lead throughout the bone. The largest variations cannot be considered to be an expected model of lead distributions in bone in vivo. However, if these gross variations in lead distribution can be shown to have limited effect on the determined bone lead level, then the variations expected in humans can be considered to be unimportant in the accuracy of measured bone lead levels. Utilizing the lattice design already created, lead concentrations were varied in a number of patterns. The following designs were run in MCNP for approximately 3.6 billion iterations.

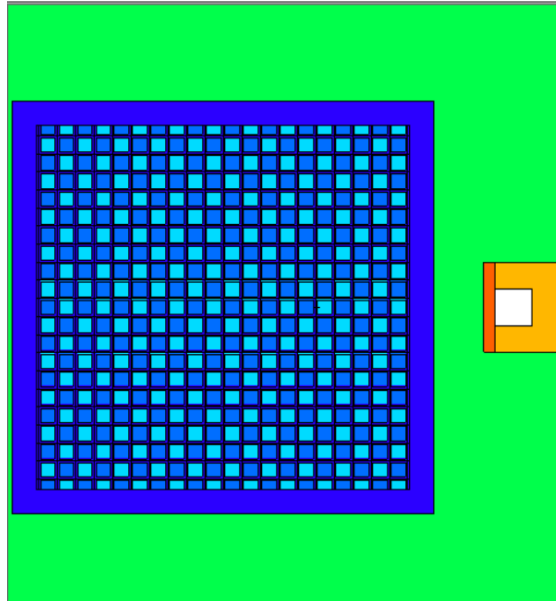


Figure 4.3 2-D view of lattice phantom “1x1” created in MCNP.

As seen in figure 4.3., describing lattice phantom “1x1”, a pattern has been created inside the lattice. The two different shades of blue represent plaster equivalent materials doped with different lead levels, one with lead, and one without. This lattice design was created using a similar design to the previously discussed lattice phantom. For this phantom and any future variations in the distribution of lead in bone, a third universe was defined. This third universe is identical in dimensions to the second universe described in creating the lattice phantom.

The difference in this universe is the material defined within, in this case, a plaster with and without lead. This allows the “fill” card to be filled with varying amounts of universe 2 (plaster with lead) and universe 3 (plaster without lead). For this design every other cube

was defined as having plaster with lead. This means that 50% of the lattice has 100 ppm Pb doped plaster, and 50% 0 ppm Pb doped plaster.

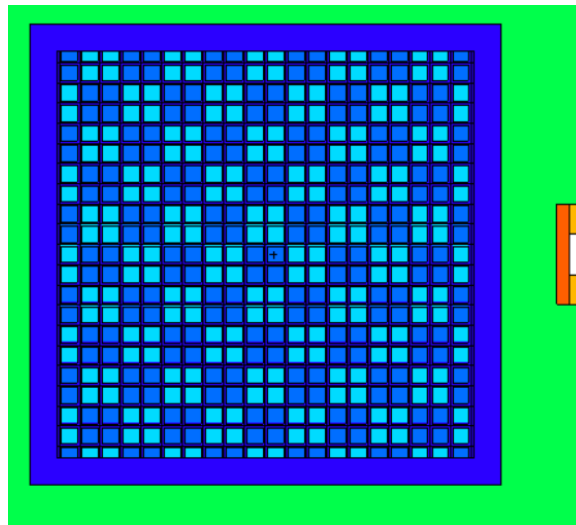


Figure 4.4 2-D view of lattice phantom “2x2” created in MCNP.

As seen in figure 4.4, building upon the “1x1” phantom design, increasingly coarser distributions of lead were created. “2x2” is named for its repeated pattern of 2 cubes defined as having plaster doped with lead, and 2 cubes of plaster defined as having plaster not doped with lead. This pattern is repeated in all dimensions, created an area of  $2^3$  cubes

Building further on this idea, a “4x4” phantom lattice was created with a coarser distribution of lead. As the name suggests, the design consists of a repeating pattern of 4 cubes defined as having plaster doped with lead, and 4 cubes of plaster defined as having plaster not doped with lead. This pattern is repeated in all dimensions, created areas of  $4^3$  cubes

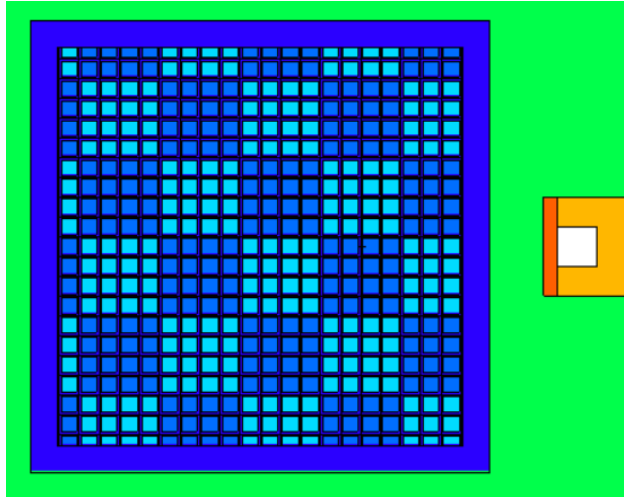


Figure 4.5 2-D view of lattice phantom “4x4” created in MCNP.

Finally, as seen in figure 4.6. below, a 11x11 phantom design was created using the same principles discussed above. The “11x11” phantom consists of 11 cubes defined as having plaster doped with lead and 11 cubes defined as having plaster not doped with lead. This cube is as far as this design path can be taken since the total number of cubes in the system is  $22^3$ .

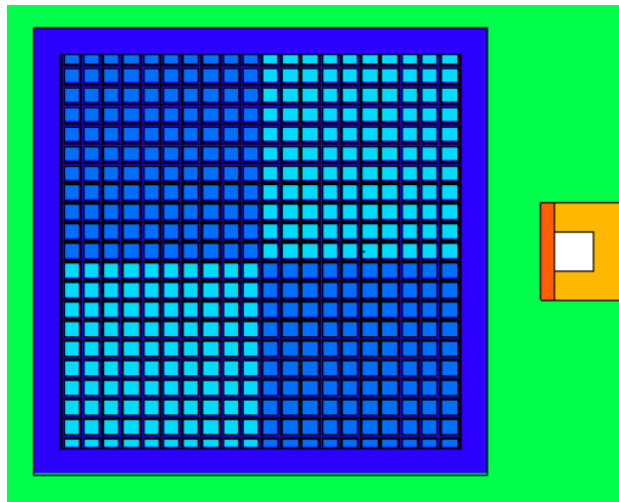


Figure 4.6 2-D view of lattice phantom “11x11” created in MCNP.

### 4.3. Testing the effect of tissue overlay in obese subjects in MCNP

To test if significant soft tissue can have an effect of the Pb  $K_{\alpha 1}$  peak area/coherent peak area for XRF measurements, phantom designs were created in MCNP with a variety of tissue equivalent thicknesses. These phantoms are cylindrical plastic containers filled with plaster of Paris. The phantom dimensions are 25mm radius, 70mm height, placed 6mm from the source. The thickness of tissue surrounding the bone was increased from 0 cm to 5 cm in increments of 0.5 cm. The distance from the edge of the phantom to the source remained constant. These simulations were run for approximately 6 billion iterations.

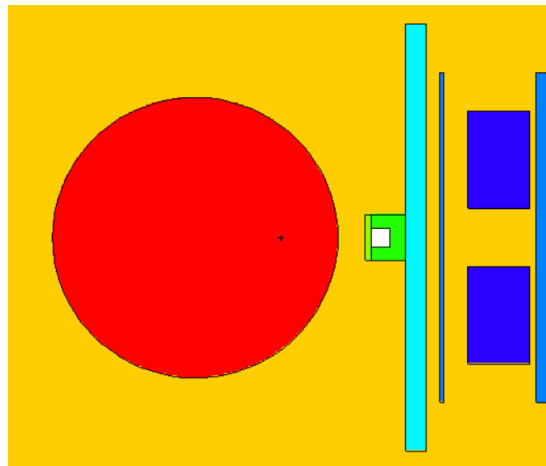


Figure 4.7 2-D view of cylindrical plaster phantom with 0 cm of soft tissue created in MCNP

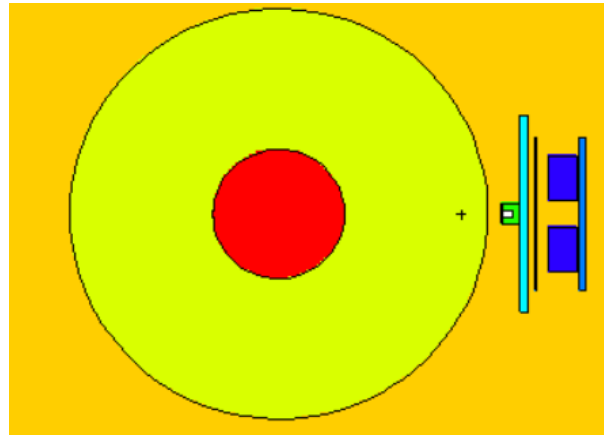


Figure 4.8 2-D view of cylindrical plaster phantom with 5 cm of soft tissue created in MCNP

## 5. Results and Discussion of Monte Carlo Simulations of Porous Bone Phantom

### 5.1. MCNP simple tibia phantom measurements and calibration line

MCNP, a Monte-Carlo simulation software, was used to verify and expand on the results seen experimentally. The cylindrical phantoms were recreated in the code to be used as a baseline for comparison with the lattice phantom designs. Phantoms were created with concentrations between 0 and 100 ppm and each input file was run for approximately 6 billion iterations. Figure 5.1. shows the ratio of the Pb  $K_{\alpha 1}$  peak area/coherent peak area versus Pb concentration for detector 1. The linear regression shows an R-squared value of  $0.999 \pm 0.0015$ . The slope of this line is  $0.0046 \pm 0.00002$ , with a y intercept of  $0.0010 \pm 0.0001$ . We see this intercept is not statistically different than zero ( $P=0.38$ ) for  $n=9$  data points. An intercept of 0 is expected for this simulation as there is not possible contamination, as was observed experimentally.

However, the slope of this calibration line is not in agreement with the calibration slope observed experimentally. This is an issue that we have not been able to completely resolve as there appear to be several factors that impact the simulation. We believe there are issues with the MCNP data libraries. In the methods section, we explained that we found that the .12p data contains an incorrect K absorption edge. The data library .12p was selected for its ability to more accurately depict the coherent scatter probability. Coherent scattering is an essential part of the bone lead XRF measurement system and for this reason, a different library could not be used. A slightly higher energy had to be used for the fluorescing source. Experimentally a  $^{109}\text{Cd}$  source is used which produces an 88.035 keV gamma ray, which

is extremely useful as it is only slightly above the k-edge of Pb at 88.005 and thus maximises the photoelectric absorption cross-section. Unfortunately, the k-edge stored in MCNP in the .12p library is 88.29 keV, forcing the source energy to be increased to 88.3 keV. This changes the photoelectric cross-sections in an energy range where they are rapidly changing with energy. However, the differences in the photoelectric cross sections did not completely explain the results. We also determined problems regarding the emission probabilities of the K alpha and beta x-rays. The ratios of the K alpha 1 and K alpha 2 are not the published values, nor are the relative emissions of K alpha to K beta x-rays. The slope of the calibration line found that the ratio of the alpha peak area to coherent peak area were incorrect and further investigation of the coherent to Compton ratios found they were also different than expected. It was also not clear if the fluorescence yield being used by MCNP was the correct value, but we could not determine the value being used. Emails were sent to the MCNP code managers about these problems. They were acknowledged but were still not answered after six months.

However, although the calibration slope does not agree with experimental data, we observed that this was a constant fixed difference between MCNP and experiment. We concluded that this simulation data can still be used as intended, but only in a relative sense. That is, only MCNP data will be compared to MCNP data. The goal of these MCNP simulations is to see if any variation in results can be observed as a consequence of the phantom designs. MCNP is still useful as it allows experiment with designs that would not be possible or practical to create in the laboratory.

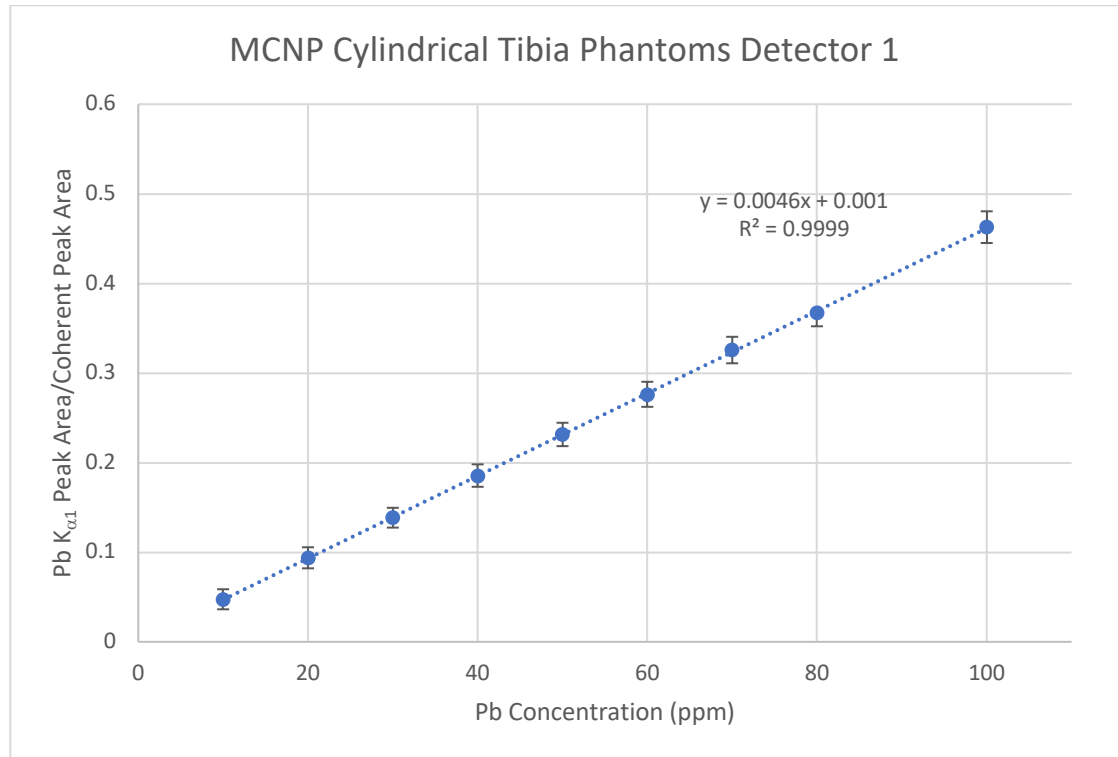


Figure 5.1 Pb concentration vs Pb  $K_{\alpha 1}$  peak area/coherent peak area for cylindrical phantom in MCNP.

Figure 5.2. show average ratio of the Pb  $K_{\alpha 1}$  peak area/coherent peak area versus the Pb concentration for all 4 detectors in the simulation. We see a R-Squared value of  $1 \pm 0.0008$ , with a slope equal to the single detector of  $0.0046 \pm 0.00001$ . This shows that all 4 detectors in the simulation are behaving in the same manner. This simulation calibration line will be used as a baseline for comparison with all future MCNP phantom designs in this thesis.

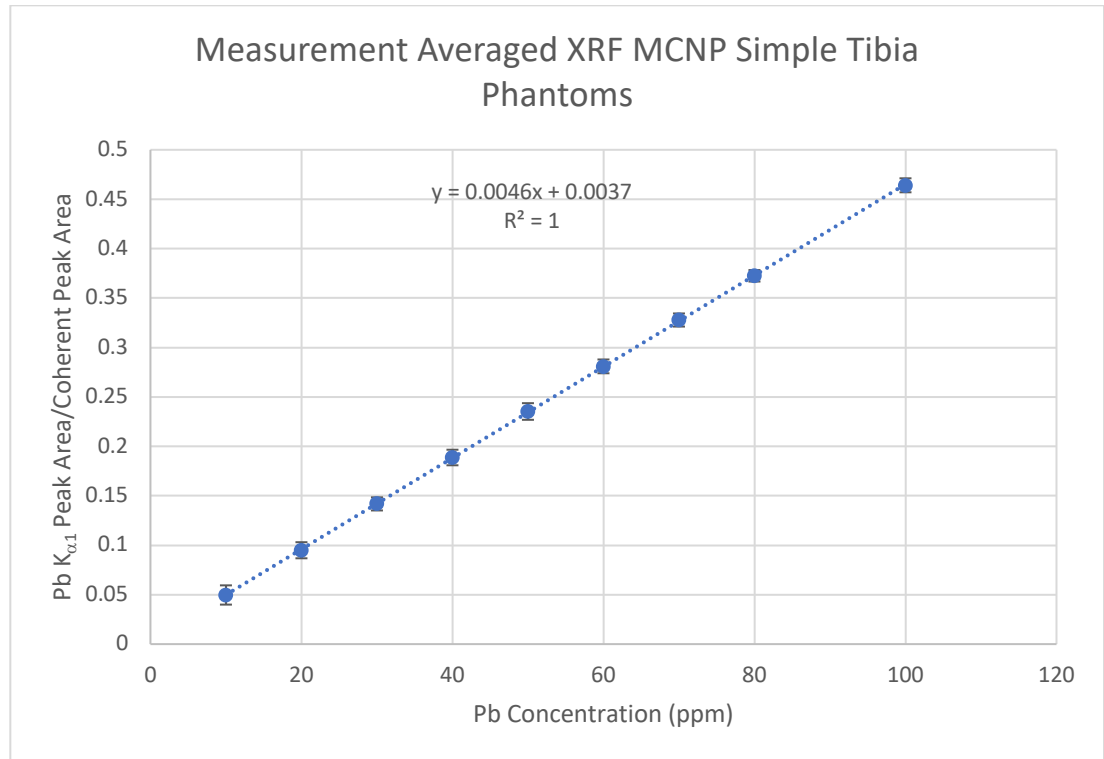


Figure 5.2 Pb concentration vs Pb K<sub>α1</sub> peak area/coherent peak area for cylindrical phantom in MCNP.

### 5.2. MCNP lattice phantom measurements and calibration line

As described in the methods section, the lattice phantom design was simulated in MCNP. This type of phantom was modelled with the same chemical compositions and physical parameters as the phantoms created in the laboratory. Five Pb concentrations were used to construct a calibration line. The 4 detector spectra were fit separately, and the results were then averaged for each concentration measurement. Based on the linear regression, we see a R-Squared value of  $0.999 \pm 0.0016$ . The line of best fit has a slope of  $0.0048 \pm 0.00002$ , with a y-intercept of  $-0.0027 \pm 0.0013$ . When comparing the slope of our cylindrical and

lattice phantoms we do observe a difference of 0.0002, however this is within the measurement uncertainty and is not statistically significantly different. Based on this information we can say that MCNP modelling agrees with the experiment: this lattice phantom design does behave differently than the traditional cylindrical phantom. The lattice, and thus we infer cortical porosity, does not perturb the measurement accuracy of a XRF bone lead measurement when the lead is homogeneously distributed.

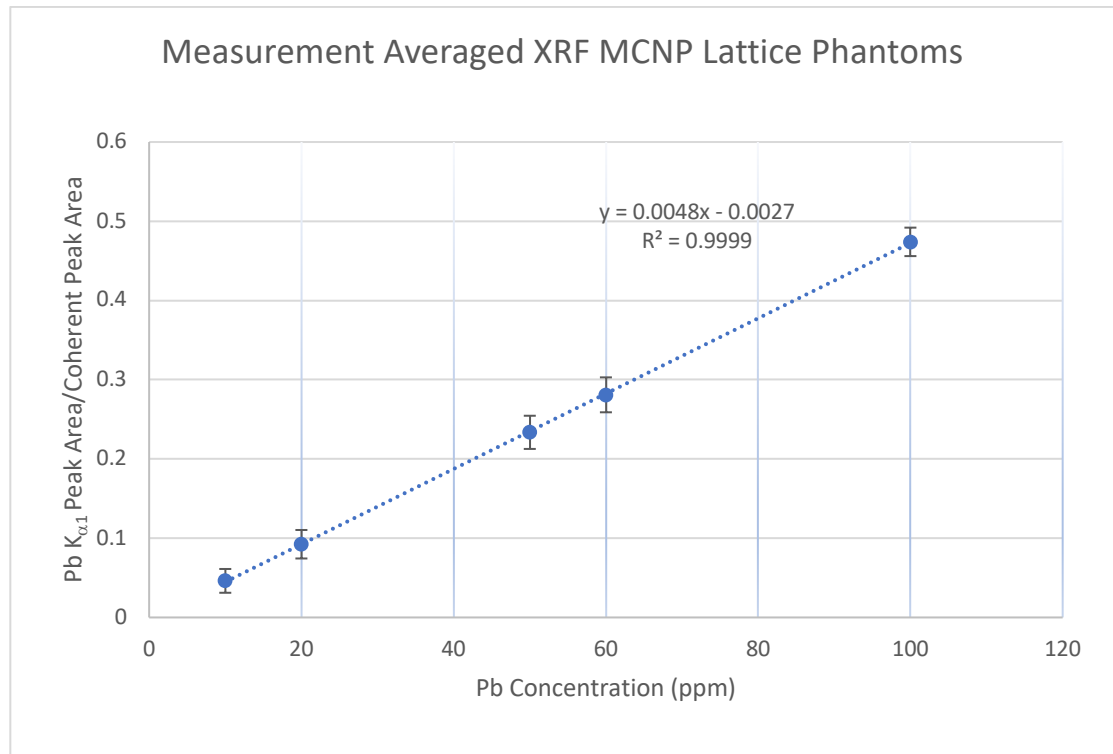


Figure 5.3 Pb concentration vs Pb K<sub>α1</sub> peak area/coherent peak area for lattice phantoms in MCNP.

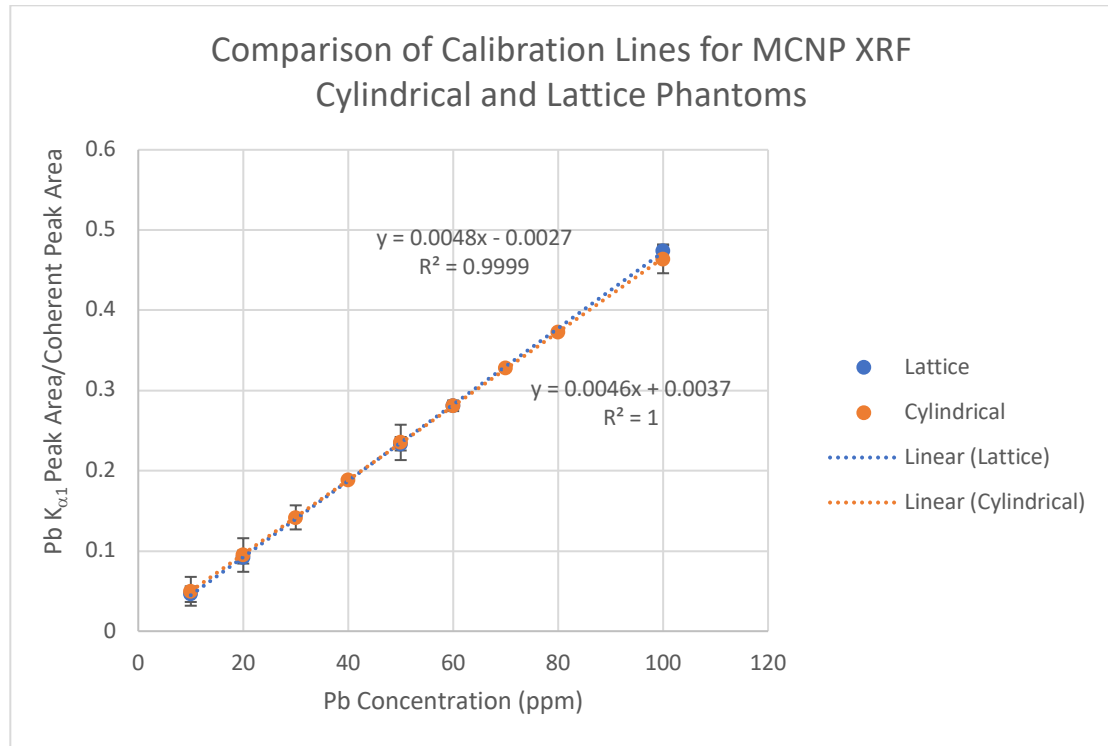


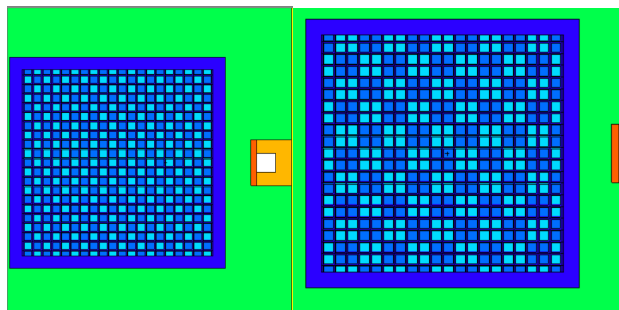
Figure 5.4 Pb concentration vs Pb  $K_{\alpha 1}$  peak area/coherent peak area for cylindrical and lattice phantoms in MCNP.

### 5.3. MCNP changes in the distribution of lead in bone

The lattice design described above uses thicker dimensions of cortical pores than those that would typically be seen in young women. This was not found to perturb the measurement so we can conclude that smaller pores should also not cause changes in measurement result. However, this result is in homogeneously distributed phantoms. Lead is not homogeneously distributed in bone, and the action of creating and filling cortical pores could cause variations in lead level throughout the bone. Therefore, further designs have been created with more extreme variations of the distribution of lead to see whether the lead distribution

in porous cortical bone can disrupt the XRF measurement results. These heterogeneous designs do not change the basic design of the lattice phantom. As outlined in the methods section X, since the design divides the phantom into equal cubic areas, which hold an equal amount of bone equivalent material, the quantity of lead in each cubic volume can be varied.

First, the lattice phantom is divided into  $22^3$  cubes. To vary the distribution of lead, these cubic areas were alternately filled with 0 or 100 ppm lead doped bone. For a visual representation of these designs see the methods section 4.2. The design can be visualized in a 2-d plane as a checkered board pattern. The distribution of cubes with and without lead remains at 50%, so the expected ratio of Pb  $K_{\alpha 1}$  peak area/coherent peak area should be equivalent to 50 ppm or 0.235 if the normalization holds true. Figure 5.6 shows the number of consecutive cubes within the phantom with Pb in the bone equivalent material vs. the Pb  $K_{\alpha 1}$  peak area/coherent peak area.



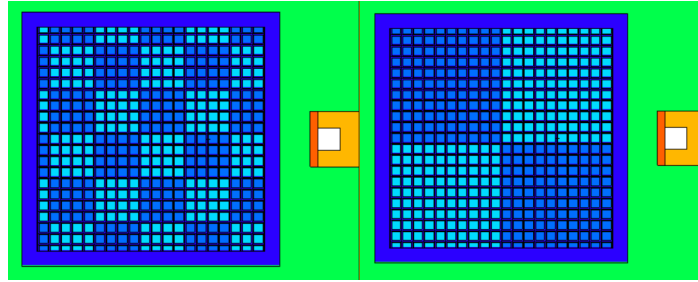


Figure 5.5 2-D view of lattice phantoms, from left to right: “1x1”, “2x2”, “4x4”, “11x11”.

The first variation tested was of alternate lead and lead-free cubes. Subsequent variations grouped the lead containing cubes together as shown in Figure 5.5.

We see from 1-4 consecutive cubes or  $1.5 \text{ mm}^3$  -  $6 \text{ mm}^3$  volumes of Pb-doped bone the normalization can still be considered to be accurate as differences are less than one standard deviation from the mean. At 11 consecutive cubes or  $16.5 \text{ mm}^3$ , the cube is divided into 8 even cubes, 4 with Pb, 4 without. At this distribution we see a ratio of Pb  $K_{\alpha 1}$  peak area/coherent peak area value which is significantly lower ( $p < 0.001$ ) than the expected value of 0.235 being  $0.11 \pm 0.018$ .

We conclude that at extreme levels of heterogeneous distributions of lead in lattice phantoms, we do see a breakdown of the accuracy of a  $^{109}\text{Cd}$  bone lead measurement as predicted by the x-ray to coherent normalization procedure. However, this level of heterogeneity of Pb distribution is likely much higher than the heterogeneity observed in human anatomy, especially in young women where the typical cortical porosity range is between 10-100 microns in diameter spaces occupying 3-7% of the surface area (Bala et al., 2014).). The non-linearities observed in the endogenous exposure relationships of blood

level to tibia level in young women aged 19 to 29 are unlikely to be measurement artifacts that are due to the effects of cortical porosity. However, one final factor needs to be explored to decide whether the endogenous exposure data has measurement artifacts: the effect of tissue overlay thickness. Many of the young women in the study were obese or even morbidly obese and had tissue overlay thicknesses higher than the average measurement subject.

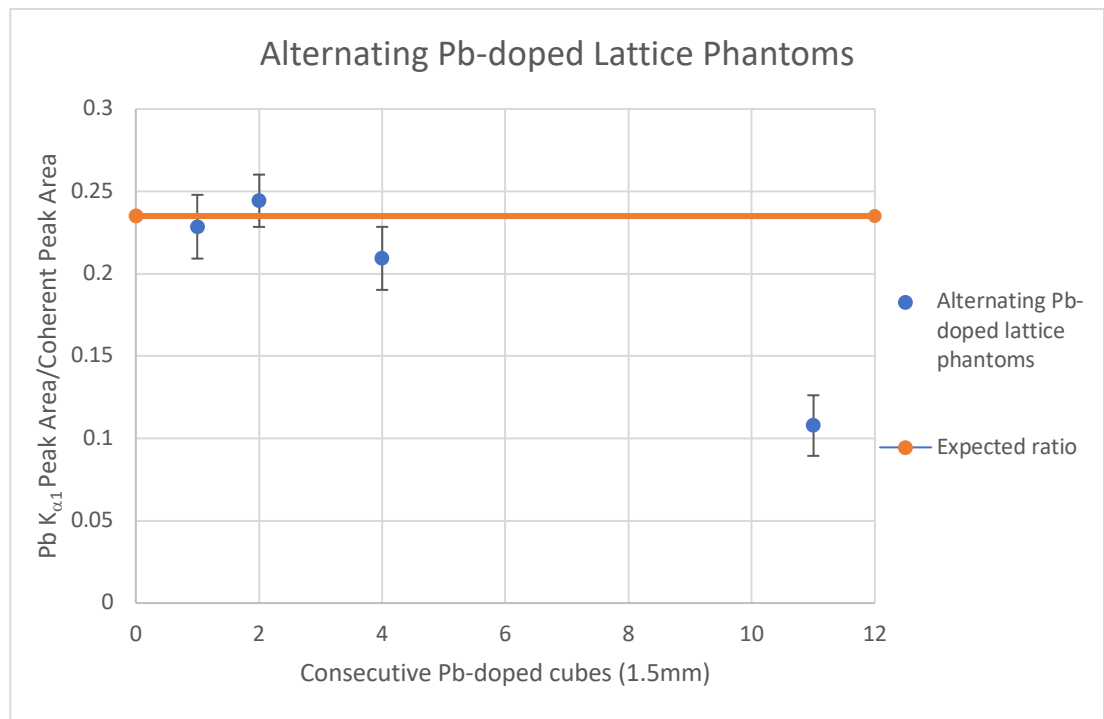


Figure 5.6 Consecutive cubes of Pb-doped bone material vs Pb  $K_{\alpha 1}$  peak area/coherent peak area for cylindrical and lattice phantoms in MCNP.

#### 5.4. Soft tissue versus alpha/coherent ratio

Cylindrical phantoms were modelled in MCNP with various tissue thicknesses, from 0 to 5 cm. Each simulation was run for approximately 6 billion iterations. The ratio of  $K_{\alpha 1}$  peak

area/coherent peak area were averaged over the 4 detectors in the simulation. Figure 6.1 shows the ratio of the Pb  $K\alpha_1$  peak area/coherent peak area versus thickness of soft tissue surrounding the cylindrical bone. As can be seen in the figure, the average ratio falls as tissue overlay thickness increases. A linear regression of this data found a slope of  $-0.0136 \pm 0.0030$ , with an intercept of  $0.4713 \pm 0.0092$ . That is, the measured lead concentration can be expected to be reduced by 2.9% ( $0.0136/0.4713 \times 100$ ) per centimetre of tissue overlay. This line showed a R-squared value of  $0.7234 \pm 0.0014$ . This slope is statistically different than zero ( $P = 0.0018$ ). A non-linear fit was found to be significantly better. As seen in figure 5.8, a second order polynomial fit improves the R-squared value to 0.9252.

However, what can be further seen in figure 6.1 is that as the thickness of soft tissue increases, so does the standard deviation of the average ratio when looking at the average across 4 detectors. We see a range of 2-25% standard deviation as the thickness increases from 0-5cm. This increase can be explained by the increased distance created by the soft tissue between the bone and the detector as well as the attenuation through the tissue. Both factors reduce the coherent signal significantly and thus increase the relative uncertainty of a measurement. It is noteworthy that although the slope is statistically significant and predicts a reduction in predicted bone lead level, the increase in the measurement uncertainty means that the predicted ratio of the  $K\alpha_1$  peak area/coherent peak for a 100-ppm phantom of  $0.4713 \pm 0.0092$  is within the standard deviation of all the measurements with a tissue thickness greater than 0 cm. In a measurement of a single individual, the reduction in predicted bone lead level would likely not be noticed.

## 6. Conclusions and Future Work

The creation of a  $^{109}\text{Cd}$  K XRF bone lead phantom which mimics the structural design of cortical porosity was found to be feasible. The use of a 3D printed design created a model that could represent cortical porosity. The limit of current 3D printing equipment available was able to create a design with structural sizes of 300 microns, representing the porous area of the bone. Higher spatial resolution 3-D printers (e.g., laser annealing 3-D resin printing) could possibly be used to create porous bone phantoms that more accurately depict the geometry of human bone.

Plaster of Paris was used in this thesis to represent the bone; this was chosen based on its historical use to create phantoms for  $^{109}\text{Cd}$  K XRF bone Pb measurement systems, as well as its low cost and ability to be poured as a solution with lead. The advantage of using plaster of Paris here was that a set of bone lead calibration phantoms could be created to determine if the cortical porosity phantom design would behave similarly to past plaster of Paris bone lead phantoms when measured with the K-XRF bone lead system at McMaster. It was determined that this new design did not behave differently than previous bone lead phantoms ( $p=0.37$ ) for  $n=6$ . While plaster of Paris was useful for this work, it is not a perfect representation of bone. Other researchers have created calibration phantoms for elements such as gadolinium using calcium hydroxyapatite as the phantom bone matrix. These hydroxyapatite phantoms are made using a liquid phase. Future phantoms may wish to consider the use of 3-D printed soft tissue with the matrix infilled with doped calcium hydroxyapatite as a more accurate representation of bone.

In order to verify these results, MCNP, a Monte-Carlo simulation software was used to recreate the XRF system and phantom designs. To create a baseline for future comparison, the simplistic

cylindrical phantom design created experimentally was recreated in MCNP. Using these simulations, calibration lines were created, based on the average  $K_{\alpha 1}$  peak area/coherent peak area of all 4 detectors, and a calibration line with a slope of  $0.0046 \pm 0.00001$  and a R-squared value of  $1 \pm 0.0008$  was found. This slope was found to be significantly different than the slope obtained experimentally. A number of problems were found in the MCNP data libraries. The lead K absorption edge was found to be at the wrong energy: it was found to be 300 eV too high. The relative intensities of the K x-rays appeared to be incorrect and there may be problems with the code's predicted fluorescence yield. While newer data libraries appear to have fixed these issues, they have not been fixed in the libraries with accurate coherent scatter data. Researchers should use up to date libraries if they are modelling x-ray fluorescence only. Caution should be taken when modelling coherent scattering. The accuracy of other x-ray Monte Carlo codes should probably be explored.

While there were problems using comparisons of MCNP to experiment, comparisons of MCNP to MCNP appeared to be consistent. The lattice phantom design was then recreated in MCNP, and calibration lines were created for comparison with the historical phantom design. The difference between the historical phantoms and the lattice phantom were found to therefore not be statistically significant. Cortical porosity does not appear to affect  $^{109}\text{Cd}$  K XRF measurements of homogeneously distributed lead in bone. This simulation is for the specific case of  $^{109}\text{Cd}$  K XRF of bone and studies will need to be performed of other elements to determine whether this remains true in those cases.

To further investigate if the distribution of lead within bone can affect K-XRF bone lead measurements, designs were created in MCNP with varied distributions up to exaggerated changes. It was shown that at extreme variations in the distributions of lead, the accuracy of the  $^{109}\text{Cd}$  bone lead system does breakdown. This, however, is for distributions far above what would typically be seen in humans, especially young woman. These models suggest that cortical porosity does not produce an artifact. However, these results cannot be extrapolated to other distributions. For example, in children, lead might be expected to be found at much higher levels at the outer bone surface. Further modelling would be required to study the effect of this different distribution.

This thesis found that significant soft tissue overlay can have an effect on the accuracy of K-XRF bone lead measurements. Studies conducted in MCNP of cylindrical phantoms with varying soft tissue thicknesses found that the average  $K_{\alpha 1}$  peak area/coherent peak area decreased as soft tissue thickness increased. A non-linear fit showed a line of best of fit of a polynomial function as seen in figure 6.2, with an R squared value of 0.925.

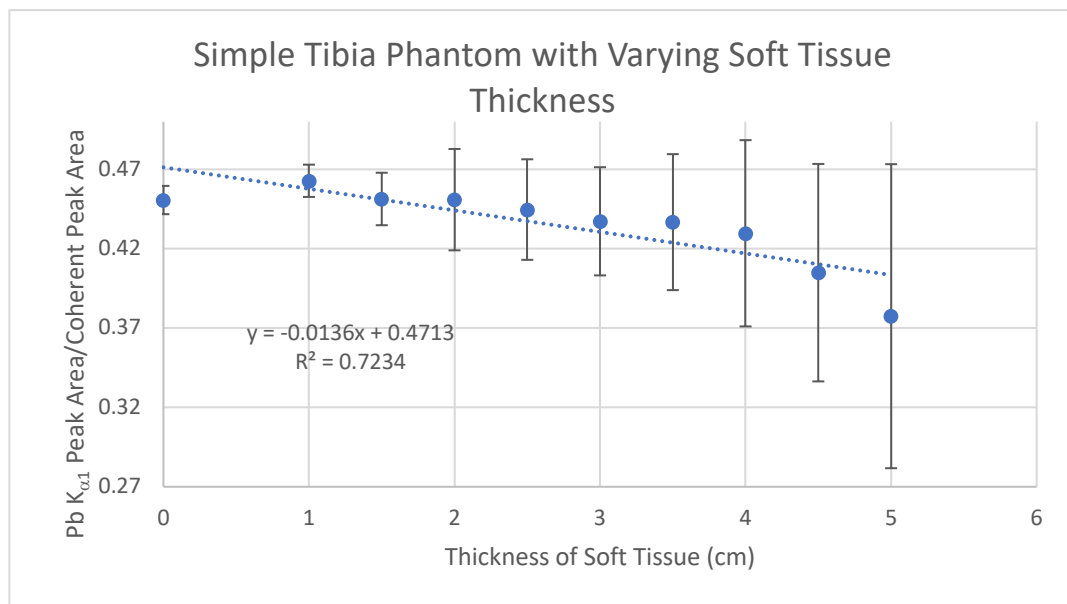


Figure 6.1 Thickness of soft tissue vs. Pb  $K_{\alpha 1}$  peak area/coherent peak area.

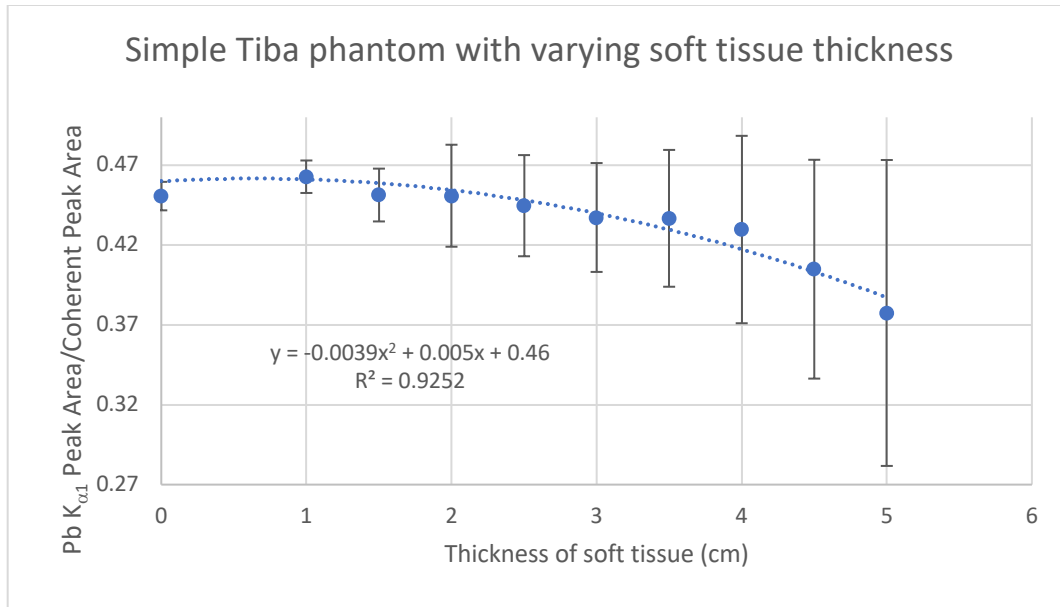


Figure 6.2 Thickness of soft tissue vs. Pb  $K_{\alpha 1}$  peak area/coherent peak area with non-linear fit.

In the studies of young women conducted in 1994, tissue overlay thickness was not measured but body mass index was assessed. Figure 6.2 below shows average bone lead level for groups of women of varied body mass index. As these women are all drawn from the same population, the average bone lead level of each group should be the same. However, as body mass index increases, the measured bone lead level decreases in women with an average BMI of 40. These results show a similar pattern as to what is seen versus above in figure 6.1. The best fit to the bone lead level versus body mass index is also a polynomial function with an  $R^2$  value of 0.98. Given that BMI may be a surrogate measure for tissue overlay thickness, and x-ray/coherent ratio can be converted to bone lead level, these two figures are possibly indicating the same thing.

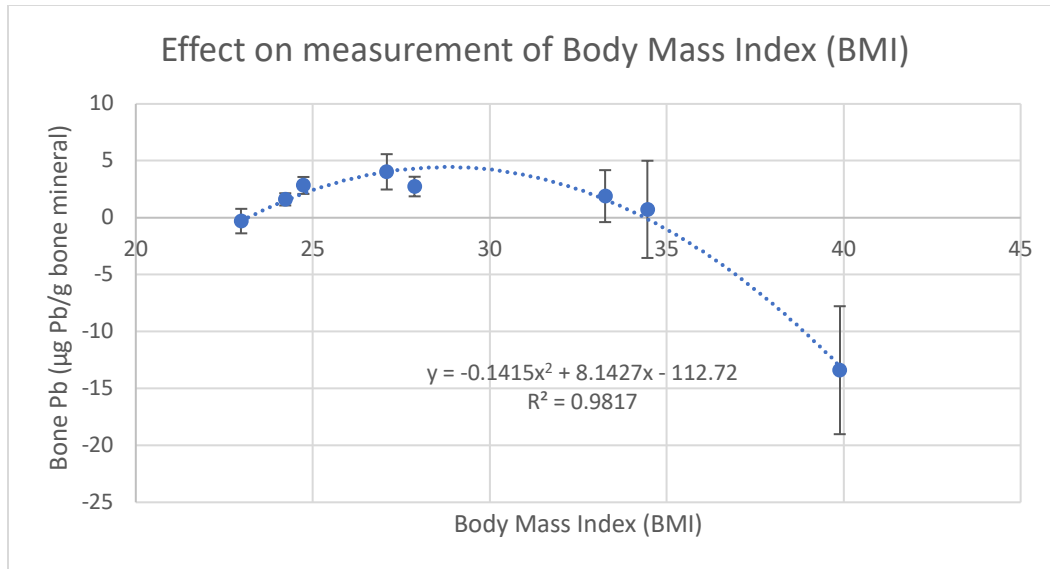


Figure 6.3 Bone Pb ( $\mu\text{g Pb/g bone mineral}$ ) versus Body Mass Index.

While x-ray to coherent ratio can be converted to bone lead level, there are no data for the relationship of tibia tissue overlay thickness to BMI in women. The two charts cannot be converted to be compared directly. However, the similarities are suggestive. The explanation for the decrease in bone lead level observed in high BMI individuals is probably that the large soft tissue mass contributes significantly to the coherent signal and disrupts the normalization. This should be explored in greater depth in future studies.

## Bibliography

- Ahlgren, L., So, M., & Mattsson, S. (1979). *An X-ray Fluorescence Technique for in vivo Determination of Lead Concentration in a Bone Matrix*. *24*(1), 136–145.
- Anderson, C., & Danylchuk, K. D. (1977). The effect of chronic low level lead intoxication on the Haversian remodeling system in dogs. *Laboratory Investigation; a Journal of Technical Methods and Pathology*, *37*(5), 466–469. <https://europepmc.org/article/med/916621>
- Bala, Y., Zebaze, R., Ghasem-Zadeh, A., Atkinson, E. J., Iuliano, S., Peterson, J. M., Amin, S., Bjørnerem, Å., Melton, L. J., Johansson, H., Kanis, J. A., Khosla, S., & Seeman, E. (2014). Cortical Porosity Identifies Women with Osteopenia at Increased Risk for Forearm Fractures. *Journal of Bone and Mineral Research: The Official Journal of the American Society for Bone and Mineral Research*, *29*(6), 1356. <https://doi.org/10.1002/JBMR.2167>
- Barry, P. S. I. (1975). A comparison of concentrations of lead in human tissues. *British Journal of Industrial Medicine*, *32*(2), 119–139. <https://doi.org/10.1136/OEM.32.2.119>
- Behinaein, S., Chettle, D. R., Atanackovic, J., Egden, L. M., Fleming, D. E. B., Nie, L. H., Richard, N., & Stever, S. (2011). In vivo measurement of lead in the bones of smelter workers using the four-element “clover-leaf” geometry detector system. *Physics in Medicine and Biology*, *56*(3), 653–665. <https://doi.org/10.1088/0031-9155/56/3/008>
- Bose, S., Vahabzadeh, S., & Bandyopadhyay, A. (2013). Bone tissue engineering using 3D printing. *Materials Today*, *16*(12), 496–504. <https://doi.org/10.1016/J.MATTOD.2013.11.017>
- Burghardt, A. J., Kazakia, G. J., Ramachandran, S., Link, T. M., & Majumdar, S. (2010). Age- and gender-related differences in the geometric properties and biomechanical significance of intracortical porosity in the distal radius and tibia. *Journal of Bone and Mineral Research*:

- The Official Journal of the American Society for Bone and Mineral Research*, 25(5), 983–993. <https://doi.org/10.1359/JBMR.091104>
- Burt, L. A., Macdonald, H. M., Hanley, D. A., & Boyd, S. K. (2014). Bone microarchitecture and strength of the radius and tibia in a reference population of young adults: an HR-pQCT study. *Archives of Osteoporosis*, 9, 183. <https://doi.org/10.1007/S11657-014-0183-2>
- Cardoso, L., Fritton, S. P., Gailani, G., Benalla, M., & Cowin, S. C. (2013). Advances in assessment of bone porosity, permeability and interstitial fluid flow. *Journal of Biomechanics*, 46(2), 253–265. <https://doi.org/10.1016/J.JBIOMECH.2012.10.025>
- Chettle, D. R., & McNeill, F. E. (2019). Elemental analysis in living human subjects using biomedical devices. *Physiological Measurement*, 40(12), 12TR01. <https://doi.org/10.1088/1361-6579/AB6019>
- Christoffersson, J. O., Schütz, A., Ahlgren, L., Haeger-Aronsen, B., Mattsson, S., & Skerfving, S. (1984). Lead in finger-bone analysed in vivo in active and retired lead workers. *American Journal of Industrial Medicine*, 6(6), 447–457. <https://doi.org/10.1002/AJIM.4700060608>
- Cooper, D. M. L., Kawalilak, C. E., Harrison, K., Johnston, B. D., & Johnston, J. D. (2016). Cortical Bone Porosity: What Is It, Why Is It Important, and How Can We Detect It? *Current Osteoporosis Reports*, 14(5), 187–198. <https://doi.org/10.1007/s11914-016-0319-y>
- Cooper, D. M. L., Thomas, C. D. L., Clement, J. G., & Hallgrímsson, B. (2006). Three-dimensional microcomputed tomography imaging of basic multicellular unit-related resorption spaces in human cortical bone. *The Anatomical Record. Part A, Discoveries in Molecular, Cellular, and Evolutionary Biology*, 288(7), 806–816. <https://doi.org/10.1002/AR.A.20344>

- Cooper, D. M. L., Turinsky, A. L., Sensen, C. W., & Hallgrímsson, B. (2003). Quantitative 3D analysis of the canal network in cortical bone by micro-computed tomography. *The Anatomical Record Part B: The New Anatomist*, 274B(1), 169–179. <https://doi.org/10.1002/AR.B.10024>
- Craswell, P. W., Price, J., Boyle, P. D., Heazlewood, V. J., Baddeley, H., Lloyd, H. M., Thomas, B. J., & Thomas, B. W. (1984). Chronic renal failure with gout: A marker of chronic lead poisoning. *Kidney International*, 26(3), 319–323. <https://doi.org/10.1038/KI.1984.175>
- Datta, H. K., Ng, W. F., Walker, J. A., Tuck, S. P., & Varanasi, S. S. (2008). The cell biology of bone metabolism. *Journal of Clinical Pathology*, 61(5), 577–587. <https://doi.org/10.1136/JCP.2007.048868>
- Gerr, F., Letz, R., Stokes, L., Chettle, D., McNeill, F., & Kaye, W. (2002). Association between bone lead concentration and blood pressure among young adults. *American Journal of Industrial Medicine*, 42(2), 98–106. <https://doi.org/10.1002/AJIM.10096>
- Gordon, C. L., Chettle, D. R., & Webber, C. E. (1993). An improved instrument for the in vivo detection of lead in bone. *British Journal of Industrial Medicine*, 50(7), 637–641. <https://doi.org/10.1136/oem.50.7.637>
- Hughes, H. G. (2014). *Enhanced Electron-Photon Transport in MCNP6*. 03105. <https://doi.org/10.1051/SNAMC/201403105>
- Hursh, J. B. (1973). Retention of <sup>210</sup>Pb in beagle dogs. *Health Physics*, 25(1), 29–35. <https://doi.org/10.1097/00004032-197307000-00003>
- Jamali, A., Hilpert, A., Debes, J., Afshar, P., Rahban, S., & Holmes, R. (2002). Hydroxyapatite/Calcium Carbonate (HA/CC) vs. Plaster of Paris: A Histomorphometric and

- Radiographic Study in a Rabbit Tibial Defect Model. *Calcified Tissue International* 2002 71:2, 71(2), 172–178. <https://doi.org/10.1007/S00223-001-1087-X>
- Keldani, Z., Lord, M. L., McNeill, F. E., Chettle, D. R., & Grafe, J. L. (2017). Coherent normalization for in vivo measurements of gadolinium in bone. *Physiological Measurement*, 38(10), 1848–1858. <https://doi.org/10.1088/1361-6579/aa87f0>
- Leggett, R. W. (1993). Research advances: An age-specific kinetic model of lead metabolism in humans. *Environmental Health Perspectives*, 101(7), 598–616. <https://doi.org/10.1289/EHP.93101598>
- M.J. Berger, J.H. Hubbell, S.M. Seltzer, J. Chang, J.S., Coursey, R. Sukumar, D.S. Zucker, & K. Olsen. (2010). *NIST Standard Reference Database 8 (XGAM)*. National Institute of Standards and Technology. <http://physics.nist.gov/xcom>
- Morgan, E. F., & Gerstenfeld, L. C. (2020). The bone organ system: Form and function. *Marcus and Feldman's Osteoporosis*, 15–35. <https://doi.org/10.1016/B978-0-12-813073-5.00002-2>
- Needleman, H. L., Riess, J. A., Tobin, M. J., Biesecker, G. E., & Greenhouse, J. B. (1996). Bone Lead Levels and Delinquent Behavior. *JAMA*, 275(5), 363–369. <https://doi.org/10.1001/JAMA.1996.03530290033034>
- Nie, H., Chettle, D., Luo, L., & O'Meara, J. (2006a). In vivo investigation of a new  $^{109}\text{Cd}$   $\gamma$ -ray induced K-XRF bone lead measurement system. *Physics in Medicine and Biology*, 51(2), 351–360. <https://doi.org/10.1088/0031-9155/51/2/011>
- Nie, H., Chettle, D., Luo, L., & O'Meara, J. (2006b). In vivo investigation of a new  $^{109}\text{Cd}$   $\gamma$ -ray induced K-XRF bone lead measurement system. *Physics in Medicine and Biology*, 51(2), 351–360. <https://doi.org/10.1088/0031-9155/51/2/011>

- Nilsson, U., Attewell, R., Christoffersson, J. -O, Schütz, A., Ahlgren, L., Skerfving, S., & Mattsson, S. (1991). Kinetics of Lead in Bone and Blood after End of Occupational Exposure. *Pharmacology & Toxicology*, 68(6), 477–484. <https://doi.org/10.1111/J.1600-0773.1991.TB01273.X>
- Nishiyama, K. K., & Shane, E. (2013). Clinical Imaging of Bone Microarchitecture with HR-pQCT. *Current Osteoporosis Reports*, 11(2), 147. <https://doi.org/10.1007/S11914-013-0142-7>
- Pemmer, B., Roschger, A., Wastl, A., Hofstaetter, J. G., Wobrauschek, P., Simon, R., Thaler, H. W., Roschger, P., Klaushofer, K., & Strelci, C. (2013). Spatial distribution of the trace elements zinc, strontium and lead in human bone tissue. *Bone*, 57(1), 184–193. <https://doi.org/10.1016/j.bone.2013.07.038>
- Popovic, M., McNeill, F. E., Chettle, D. R., Webber, C. E., Lee, C. V., & Kaye, W. E. (2005). Impact of occupational exposure on lead levels in women. *Environmental Health Perspectives*, 113(4), 478–484. <https://doi.org/10.1289/EHP.7386>
- Schwartz, B. S., Lee, B., Bandeen-Roche, K., Stewart, W., Bolla, K., Links, J., Weaver, V., & Todd, A. (2005). Occupational Lead Exposure and Longitudinal Decline in Neurobehavioral Test Scores on JSTOR. *Epidemiology*, 16(1), 106–112. <https://www.jstor.org/stable/20486007>
- Seitz, H., Rieder, W., Irsen, S., Leukers, B., & Tille, C. (2005). Three-dimensional printing of porous ceramic scaffolds for bone tissue engineering. *Journal of Biomedical Materials Research - Part B Applied Biomaterials*, 74(2), 782–788. <https://doi.org/10.1002/JBM.B.30291>

- Smith, D. W., Gardiner, B. S., & Dunstan, C. (2012). Bone Balance within a Cortical BMU: Local Controls of Bone Resorption and Formation. *PLOS ONE*, 7(7), e40268. <https://doi.org/10.1371/JOURNAL.PONE.0040268>
- Somervaille, L. J., Chettle, D. R., & Scott, M. C. (1985). In vivo measurement of lead in bone using X-ray fluorescence. *Physics in Medicine & Biology*, 30(9), 929. <https://doi.org/10.1088/0031-9155/30/9/005>
- Stokes, L., Letz, R., Gerr, F., Kolczak, M., McNeill, F. E., Chettle, D. R., & Kaye, W. E. (1998). Neurotoxicity in young adults 20 years after childhood exposure to lead: the Bunker Hill experience. *Occupational and Environmental Medicine*, 55(8), 507. <https://doi.org/10.1136/OEM.55.8.507>
- Tofail, S. A. M., Koumoulos, E. P., Bandyopadhyay, A., Bose, S., O'Donoghue, L., & Charitidis, C. (2018). Additive manufacturing: scientific and technological challenges, market uptake and opportunities. *Materials Today*, 21(1), 22–37. <https://doi.org/10.1016/J.MATTOD.2017.07.001>
- Trojek, T., & Čechák, T. (2007). Use of MCNP code in energy dispersive X-ray fluorescence. *Nuclear Instruments and Methods in Physics Research Section B: Beam Interactions with Materials and Atoms*, 263(1), 72–75. <https://doi.org/10.1016/J.NIMB.2007.04.063>
- van den Bergh, J. P., Szulc, P., Cheung, A. M., Bouxsein, M., Engelke, K., & Chapurlat, R. (2021). The clinical application of high-resolution peripheral computed tomography (HR-pQCT) in adults: state of the art and future directions. *Osteoporosis International: A Journal Established as Result of Cooperation between the European Foundation for Osteoporosis and the National Osteoporosis Foundation of the USA*, 32(8), 1465–1485. <https://doi.org/10.1007/S00198-021-05999-Z>

- Vilayphiou, N., Boutroy, S., Sornay-Rendu, E., van Rietbergen, B., & Chapurlat, R. (2016). Age-related changes in bone strength from HR-pQCT derived microarchitectural parameters with an emphasis on the role of cortical porosity. *Bone*, *83*, 233–240. <https://doi.org/10.1016/J.BONE.2015.10.012>
- Wani, A. L., Ara, A., & Usmani, J. A. (2015). Lead toxicity: a review. *Interdisciplinary Toxicology*, *8*(2), 55. <https://doi.org/10.1515/INTOX-2015-0009>
- Weisskopf, M. G., Weuve, J., Nie, H., Saint-Hilaire, M. H., Sudarsky, L., Simon, D. K., Hersh, B., Schwartz, J., Wright, R. O., & Hu, H. (2010). Association of Cumulative Lead Exposure with Parkinson's Disease. *Environmental Health Perspectives*, *118*(11), 1609–1613. <https://doi.org/10.1289/EHP.1002339>
- Werner, C. J. (2018). *MCNP User's Manual Code Version 6.2*.